MNRAS **000**, 1–18 (2016) Preprint 27 September 2016 Compiled using MNRAS LATEX style file v3.0

Galaxy Simulation with Dust Formation and Destruction

Shohei Aoyama,[1,2⋆] Kuan-Chou Hou,[3,4] Ikkoh Shimizu,[1,2] Hiroyuki Hirashita,[3] Keita Todoroki,[5,6] Jun-Hwan Choi,[7] and Kentaro Nagamine[1,6]

[1] *Theoretical Astrophysics, Department of Earth & Space Science, Osaka University, 1-1 Machikaneyama, Toyonaka, Osaka 560-0043, Japan*
[2] *College of General Education, Osaka Sangyo University, 3-1-1, Nakagaito, Daito, Osaka, 574-8530, Japan*
[3] *Institute of Astronomy, and Astrophysics, Academia Sinica, PO Box 23-141, Taipei 10617, Taiwan*
[4] *Department of Physics & Institute of Astrophysics, National Taiwan University, Taipei 10617, Taiwan*
[5] *Department of Physics & Astronomy, University of Kansas,1082 Malott,1251 Wescoe Hall Dr., Lawrence, KS 66045-758, USA*
[6] *Department of Physics & Astronomy, University of Nevada, Las Vegas, 4505 S. Maryland Pkwy, Las Vegas, NV 89154-4002, USA*
[7] *Department of Astronomy, University of Texas Austin, TX 78712-1205, USA*

arXiv:1609.07547v1 [astro-ph.GA] 24 Sep 2016

Accepted XXX. Received YYY; in original form ZZZ

ABSTRACT

We perform smoothed particle hydrodynamics (SPH) simulations of an isolated galaxy with a new treatment for dust formation and destruction. To this aim, we treat dust and metal production self-consistently with star formation and supernova feedback. For dust, we consider a simplified model of grain size distribution by representing the entire range of grain sizes with large and small grains. We include dust production in stellar ejecta, dust destruction by supernova (SN) shocks, grain growth by accretion and coagulation, and grain disruption by shattering. We find that the assumption of fixed dust-to-metal mass ratio becomes no longer valid when the galaxy is older than 0.2 Gyr, at which point the grain growth by accretion starts to contribute to the nonlinear rise of dust-to-gas ratio. As expected in our previous one-zone model, shattering triggers grain growth by accretion since it increases the total surface area of grains. Coagulation becomes significant when the galaxy age is greater than ~ 1 Gyr: at this epoch the abundance of small grains becomes high enough to raise the coagulation rate of small grains. We further compare the radial profiles of dust-to-gas ratio ($\mathcal{D}$) and dust-to-metal ratio ($\mathcal{D}/Z$) (i.e., depletion) at various ages with observational data. We find that our simulations broadly reproduce the radial gradients of dust-to-gas ratio and depletion. In the early epoch ($\lesssim 0.3$ Gyr), the radial gradient of $\mathcal{D}$ follows the metallicity gradient with $\mathcal{D}/Z$ determined by the dust condensation efficiency in stellar ejecta, while the $\mathcal{D}$ gradient is steeper than the Z gradient at the later epochs because of grain growth by accretion. The framework developed in this paper is applicable to any SPH-based galaxy evolution simulations including cosmological ones.

Key words: methods: numerical – ISM: dust – galaxies: evolution – galaxies: formation – galaxies: ISM – galaxies: general

1 INTRODUCTION

The importance of cosmic dust in astrophysical processes has been recognized in recent decades. Dust acts as an efficient catalyst of molecular hydrogen (H_2) formation in the interstellar medium (ISM) (e.g., Gould & Salpeter 1963; Cazaux & Tielens 2004; Cazaux & Spaans 2009). In addition, the typical mass of the final fragments in star-forming clouds is also regulated by dust cooling (Whitworth et al. 1998; Larson 2005; Omukai et al. 2005; Schneider et al. 2006). In protoplanetary discs, dust growth eventually leads to planet formation (e.g., Okuzumi et al. 2009; Kataoka et al. 2014). Dust grains also play an important role in radiative processes in the ISM by absorbing stellar light and reemitting it in the far-infrared, and change the spectral energy distributions of galaxies (Calzetti et al. 2000; Buat et al. 2002; Takeuchi et al. 2012).

For the dust properties in galaxies, the size distribution of dust grains is of fundamental importance (e.g., Mathis et al. 1977; Nozawa & Fukugita 2013). In particular, the extinction curve (i.e., the wavelength dependence of absorption and scattering cross-section) is shaped by the grain size distribution, given the grain materials (Bohren et al. 1983). Precise estimates of star formation rate (SFR) in galaxies also require correction for dust extinction (e.g., Steidel et al. 1999; Takeuchi et al. 2010; Kennicutt & Evans 2012). In ad-

⋆ E-mail: aoyama@vega.ess.sci.osaka-u.ac.jp (SA)

© 2016 The Authors

dition, the total dust surface area which depends on the grain size distribution governs the formation rate of molecular hydrogen (e.g., Barlow & Silk 1976; Yamasawa et al. 2011).

Dust interacts with gas, metals and dust itself in the ISM. It is not only destroyed by supernova (SN) shocks, but also disrupted or shattered by grain-grain collisions in the diffuse ISM (Yan et al. 2004). In dense environments such as molecular clouds, it grows by accretion and coagulation (Hirashita & Voshchinnikov 2014; Voshchinnikov & Hirashita 2014). All these processes play important roles in the evolution of dust abundance and grain size distribution.

Asano et al. (2013b) have established a full framework for treating the evolution of grain size distribution consistently with the chemical enrichment in a galaxy. Their work revealed that the collisional effects of dust grains such as coagulation, shattering, and accretion are necessary for a comprehensive understanding of the observed dust-to-gas mass ratio and extinction curves in nearby galaxies. However, Asano et al. (2013b) treated a galaxy as a single zone without taking into account the spatial distribution of gas with different density structures. Since the efficiencies of various dust processing mechanisms depend on the density and temperature of the ISM, hydrodynamical evolution of the ISM should also be considered simultaneously with dust evolution.

Hydrodynamical simulations have indeed been a powerful tool to clarify galaxy formation and evolution. Many cosmological hydrodynamic simulations have reproduced and predicted the observed galaxy mass and luminosity functions (e.g., Nagamine et al. 2001, 2004; Choi & Nagamine 2012; Jaacks et al. 2012, 2013; Shimizu et al. 2014; Thompson et al. 2014; Vogelsberger et al. 2014; Shimizu et al. 2015; Schaye et al. 2015). In order to compute luminosity functions from simulated galaxies and compare them with observed data, a precise estimate of dust extinction effect is required. For example, Yajima et al. (2015) calculated the galaxy UV luminosity function at high redshifts ($6 \leq z \leq 12$) using cosmological zoom-in hydrodynamical simulations with constrained initial conditions. In their work, chemistry and cooling of hydrogen, helium and metals were computed as in Choi & Nagamine (2009), however, the dust-to-metal ratio was fixed. Bekki (2015) treated dust as a new particle species in addition to gas, dark matter, and star particles. They included not only the formation and destruction of dust, but also dust-dependent star formation and stellar feedback (Bekki 2013). Furthermore, in a more recent work, McKinnon et al. (2016b) regarded dust as an additional component in gas, and performed cosmological zoom-in simulations. They revealed the importance of dust growth by the accretion of gas-phase metals, and pointed out the necessity of a more realistic treatment of dust destruction and feedback by SNe. In addition, McKinnon et al. (2016a) ran cosmological simulations and compared the dust mass function and radial profile of dust with corresponding observational data. They found that their simulation broadly reproduced the observation in the present-day Universe, although it tended to underestimate the dust abundance in high-redshift galaxies.

In all of these simulations mentioned above, dust processing by grain-grain collisions such as coagulation and shattering, both of which are important for the grain size distribution, has not been included yet (but see Zhukovska et al. 2016, who implemented part of these processes by postprocessing a hydrodynamic simulation of an isolated galaxy with a particular focus on temperature-dependent sticking coefficient). Implementation of dust size distributions in SPH simulations has not been successful, mainly because of the high computational cost. Calculating the grain size distribution in a fully self-consistent manner is computationally expensive even in one-zone calculation as shown by Asano et al. (2013b). However, because of the aforementioned effects of grain size distribution, implementation of grain size distribution in hydrodynamic simulations is essential in understanding the role of dust in galaxy evolution.

In this paper, we perform N-body/SPH simulations of isolated galaxies with a model of dust formation and destruction. For the purpose of treating the evolution of grain size distribution within a reasonable computational time, we adopt the two-size approximation formulated by Hirashita (2015), in which the entire grain size range is represented by two sizes divided at around $a \simeq 0.03$ μm, where a is the grain radius. Hirashita (2015) has confirmed that the two-size approximation gives the same evolutionary behaviour of grain sizes and extinction curves as calculated by the full treatment of Asano et al. (2013b, 2014). Thus, implementing the two-size model, which is computationally light, in hydrodynamic simulations provides a feasible way to compute the grain size evolution in the ISM. Consequently, not only can we compute the spatial variations in dust properties, but also examine the grain size distribution as a function of time and metallicity. This is a significant advantage over the simple one-zone calculations, which generally need to introduce some strong assumptions such as instantaneous mixing and homogeneity.

Although our ultimate goal is to understand dust evolution in the cosmological structure formation, the target of this paper is an isolated galaxy for the purpose of the first implementation of dust evolution. Using an isolated galaxy enables us to compare our results with previous one-zone calculations and to test our implementation. Since the spatial resolution is higher than typical cosmological simulations, we will be able to predict spatially resolved properties of dust evolution in detail.

This paper is organised as follows. In Section 2, we introduce our dust evolution model and calculation method. We present the simulation results in Section 3. We discuss the parameter dependence in Section 4 and compare the simulation results with observational data in Section 5. We conclude in Section 6. Throughout this paper, we adopt $Z_\odot = 0.02$ for solar metallicity following Hirashita (2015).

2 MODEL

2.1 Numerical Simulations

In this section, we overview our simulation setup first before we describe the details of our dust implementation. We use the modified version of `GADGET-3` N-body/SPH code (originally explained by Springel 2005), and our simulation includes dark matter, gas, and star particles. The dynamics of collisionless particles are computed with a tree-particle-mesh method, and the hydrodynamics is solved

Table 1. Initial physical parameters of our isolated galaxy. In this paper, we adopt the low-resolution model of the AGORA project (Kim et al. 2014). The disk and bulge components are pre-existing stellar components treated by collisionless star particles dynamically, but those particles are not destroyed nor created during the simulation. †The gravitational softening length is taken to be 80 pc, and we allow the baryons to collapse to 10% of this value. However, in practice, we find that the variable gas smoothing length reached a minimum value of only ∼ 22 pc with our models of gas cooling, star formation, and feedback.

Parameter	Value
Gas mass	$8.59 \times 10^9 M_\odot$
Dark matter mass	$1.25 \times 10^{12} M_\odot$
Disk mass	$4.30 \times 10^9 M_\odot$
Bulge mass	$3.44 \times 10^{10} M_\odot$
Total mass	$1.3 \times 10^{12} M_\odot$
Number of gas particle	1.00×10^5
Number of dark matter	1.00×10^5
Number of disk particle	1.00×10^5
Number of bulge particle	1.25×10^4
Gas particle mass	$8.59 \times 10^4 M_\odot$
Dark matter particle mass	$1.25 \times 10^7 M_\odot$
Disk particle mass	$3.44 \times 10^5 M_\odot$
Bulge particle mass	$3.44 \times 10^5 M_\odot$
Grav. softening length	80 pc †

with the entropy-conserving, density-independent formulation (Springel & Hernquist 2002; Saitoh & Makino 2013; Hopkins 2013), using the quintec spline kernel of Morris (1996). The star particles are stochastically created from gas particles as described in Springel & Hernquist (2003), consistently with the SFR equation which we describe below. Our code uses the Grackle[1] chemistry and cooling library (Bryan et al. 2014; Kim et al. 2014), which solves the non-equilibrium primordial chemistry network for atomic H, D, He, H_2, and HD. Using the Grackle's nonequilibrium chemistry with H_2 allows us to compute the gas properties to lower temperatures and higher densities, which is necessary for a proper treatment of dust physics as we will see below.

The initial condition of our isolated galaxy is taken from the low-resolution model of AGORA simulations (Kim et al. 2014), and various parameter values of this disc galaxy is summarised in Table 1. The highest density that we can resolve is also determined by the minimum gravitational softening length of $\epsilon_{\rm grav} = 80$ pc, and we allow the minimum gas smoothing to reach 10% of $\epsilon_{\rm grav}$. Following Hopkins et al. (2011) and Kim et al. (2016, in prep.), we adopt the Jeans pressure floor,

$$P_{\rm Jeans} = 1.2\gamma^{-1} N_{\rm Jeans}^{2/3} G\rho_{\rm gas}^2 h_{\rm sml}^2, \quad (1)$$

where $\gamma = 5/3$, $N_{\rm Jeans} = 8.75$, and $h_{\rm sml}$ is the smoothing length of gas. This is to avoid artificial numerical fragmentation when the Jeans mass at low temperatures is not resolved.

The gas particles in our simulations carry physical information such as density, internal energy, entropy, ionization fraction, metallicity, and SFR. The gas pressure can be computed from entropy and density, and the temperature from internal energy and ionization fraction. Therefore we can use these dynamically computed physical quantities to evaluate the dust processes at each point in space and time. With our new treatment for dust, the gas particles now also carry the dust mass as an additional physical parameter.

[1] https://grackle.readthedocs.org/

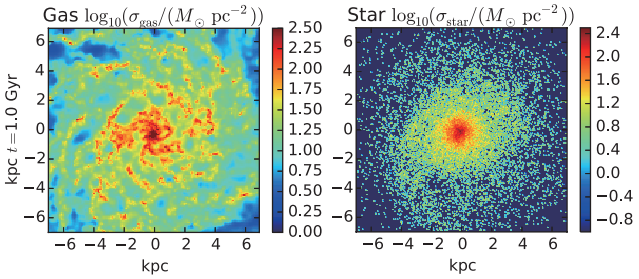

Figure 1. Face-on view of the distribution of gas surface density (left panel) and stellar surface density (right) of our simulation at $t = 1$ Gyr. The colour bar indicates the mass surface density in logarithmic units of $[M_\odot\ {\rm pc}^{-2}]$. The image was produced with a pixel size of ∼ 93 pc.

As an example, Fig. 1 shows the face-on view of surface densities of gas and stars of our simulated galaxy at $t = 1$ Gyr. Spiral arms are prominent and well developed after 1 Gyr since the beginning of the simulation, and stellar disk is clearly visible in the right panel. We also smooth the spatial distribution of metal and dust within the smoothing kernel, in a similar manner to the computation of gas density while the simulation is running.

Fig. 2 shows the overall distribution of gas in our simulated galaxy on the temperature–density plane. With our current resolution and Grackle cooling, we achieve gas number densities slightly higher than $10^4\ {\rm cm}^{-3}$ and temperatures as low as $T_{\rm gas} \sim 30$ K. There is also a distribution of tenuous gas heated by the stellar feedback effects (see Section 2.1.2) at $T_{\rm gas} > 10^5$ K, which would be absent if we turn off the feedback processes.

2.1.1 *Star Formation*

We follow the star formation prescription of the AGORA project (Kim et al. 2014). In this model, the local SFR density $d\rho_*/dt$ is estimated as

$$\frac{d\rho_*}{dt} = \varepsilon_{\rm SF} \frac{\rho_{\rm gas}}{t_{\rm ff}}, \quad (2)$$

where $\varepsilon_{\rm SF} = 0.01$ is the star formation efficiency, $\rho_{\rm gas}$ is the gas density and $t_{\rm ff} = \sqrt{3\pi/(32G\rho_{\rm gas})}$ is the local free-fall time. The star particles are stochastically created from gas particles as described in Springel & Hernquist (2003), consistently with the above SFR. But the star formation is allowed only for gas particles with $n_{\rm gas} \geq 10\ {\rm cm}^{-3}$. Each star particle is regarded as a simple stellar population with a Chabrier (2003) initial stellar mass function (IMF), and it carries stellar mass, metallicity, and formation time as its physical attributes.

Our simulation results show that the gas is converted into stars at a steady rate of $\sim 1\,M_\odot$/yr, although we do not show the figure here as it is a simple result. Total stellar mass increases monotonically from zero at $t = 0$ Gyr to 3.4×

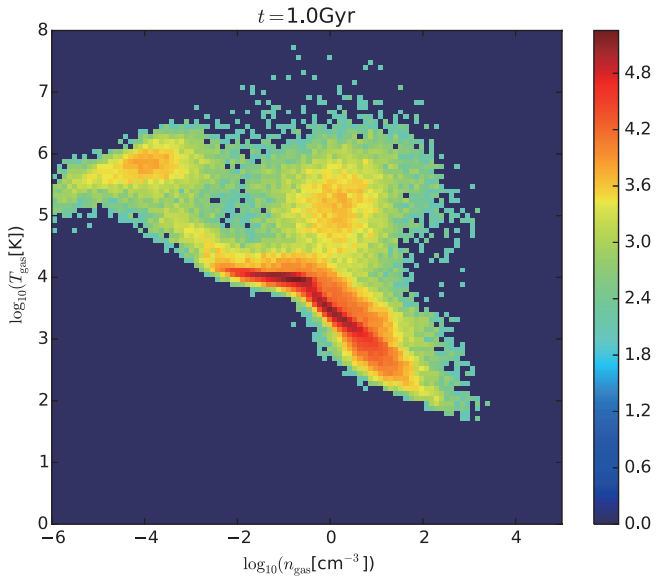

Figure 2. Distribution of gas particles on the temperature–density ($T_{\rm gas} - n_{\rm gas}$) phase diagram in our simulation at $t = 1$ Gyr. The colour indicates the logarithmic surface density of gas particles on this diagram as indicated by the colour bar on the right.

$10^9 M_\odot$ at $t = 10$ Gyr. Disk and bulge mass given Table 1 do not change as they are assumed to be made of old stellar population and treated by collisionless stellar particles. The overall gas mass of the galaxy decreases monotonically from $8.6 \times 10^9\,M_\odot$ at $t = 0$ Gyr to $5.2 \times 10^9\,M_\odot$ at $t = 10$ Gyr.

2.1.2 Early Stellar Feedback

Several studies have pointed out the impact of feedback from stellar winds and radiation of massive stars before they explode as supernovae (Wise et al. 2012; Agertz et al. 2013; Stinson et al. 2013), which is often called the 'early stellar feedback.' For example, Agertz et al. (2013) considered the momentum of ionizing radiation onto the ambient gas, and found that it is effective in sweeping up the gas in the vicinity of young star clusters. Stinson et al. (2013) also implemented a phenomenological model, which assumes that the energy from massive stars are converted and deposited among the neighbouring gas particles in a form of pure thermal energy, while turning the radiative cooling off for 30 Myrs to avoid the overcooling problem.

While our present work is more focused on the physics of dust formation and evolution, we have implement the effect of stellar feedback model, roughly following the work by Stinson et al. (2013) and Todoroki (2014). In our model, the thermal energy from early stellar feedback is injected at a constant rate for $t_{\rm explode} = 4$ Myr, which is an approximate life-time of a massive star (e.g., Fall et al. 2010). The fractional thermal energy deposited from a star particle in a single time-step is

$$\Delta E_{\rm th} = \epsilon_{\rm esf}\ E_{\rm rad}\ \frac{t - t_{\rm deposit}}{t_{\rm explode}}, \qquad (3)$$

where t is the current simulation time, $t_{\rm deposit}$ is the time at which the star deposited a fraction of the thermal energy in the previous time-step, $\epsilon_{\rm esf}$ is the early stellar feedback efficiency, and $E_{\rm rad}$ is the radiation energy which is emitted by massive stars. We adopt $E_{\rm rad} = 2 \times 10^{50}$ erg per $1\,M_\odot$ of stars (Stinson et al. 2013).

The energy $\Delta E_{\rm th}$ is then distributed among all the neighbour gas particles using the mass-weighted SPH kernel. The physical meaning of early stellar feedback efficiency, $\epsilon_{\rm esf}$, is the fraction of UV photons that contributes to the early stellar feedback. Stinson et al. (2013) find that the model with $\epsilon_{\rm esf} = 0.1$ reproduces a good agreement with the stellar-to-halo mass relation obtained from halo occupation distribution models, but here we take $\epsilon_{\rm esf} = 0.3$ to see the maximum impact of early stellar feedback. However, having examined our results on dust properties in the runs with and without the early stellar feedback, we actually find that its impact on dust results is not so strong.

2.1.3 SN model

Dust destruction by SNe is also treated by a subgrid model, as our simulations do not have the resolution to solve the gas dynamics at sub-parsec scales. In our subgrid model, we first compute a 'shock radius' ($R_{\rm sh}$) for newly formed star particles, inside which the gas particles are affected by the SN shock and the dust is destroyed. We adopt the shock radius from Chevalier (1974) and McKee & Ostriker (1977), who performed spherically symmetric hydrodynamical simulation of supernova remnant in an uniform medium. In their simulation, they considered not only the cooling via infrared, UV and X-ray radiation, but also the effects of magnetic field on the remnant. As a consequence, they obtained a shock radius as

$$R_{\rm sh} = 55.0\ [{\rm pc}] \left(\frac{E_{\rm SN}}{10^{51}\ {\rm erg}}\right)^{0.32} \times \left(\frac{n_{\rm gas}}{1\ {\rm cm}^{-3}}\right)^{-0.16} \left(\frac{P_0}{10^{-4} k_{\rm B}\ {\rm cm}^{-3}\,{\rm K}}\right)^{-0.20} \qquad (4)$$

where P_0 is the ambient pressure which is obtained by calculating the kernel-weighted mean pressure of neighbouring gas particles located within the smoothing length of the young star particle. The value of $E_{\rm SN}$, which is the total collective energy from all SNe in the star particle of concern, will be specified in equation (7).

2.1.4 Metal production and Supernova Feedback

Dust is produced from metals, and metals are ejected from supernova explosions; therefore we need to treat dust and metal production in a consistent manner with star formation and SN feedback. In this subsection, we first describe our treatment of supernova feedback and metal enrichment, which are based on the AGORA project (Kim et al. 2014) and Todoroki (2014).

We assume that stars with masses between 8 and $40 M_\odot$ explode as Type II SNe after a time-delay of $t_{\rm explode} = 4$ Myr from the star formation, and deposit a net energy of 10^{51} erg into the ambient medium. For the assumed Chabrier IMF, the number of Type II SNe per unit stellar mass is $0.011\,{M_\odot}^{-1}$. We include the effects of gas recycling and metal production from Type II SNe. We return the mass

of stars in between $8\mathrm{M}_\odot < M < 40\mathrm{M}_\odot$ into ISM after substracting the remnant mass of 1.4 $\mathrm{M}_\odot$ per star.

The total amount of metals produced and ejected from Type II SNe per stellar mass, M_Z, is calculated as

$$M_\mathrm{Z} = 2.09 M_\mathrm{O} + 1.06 M_\mathrm{Fe}, \tag{5}$$

with the corresponding fractional masses of oxygen M_O and iron M_Fe being 0.0133 $\mathrm{M}_\odot$ and 0.011 $\mathrm{M}_\odot$, respectively, per one solar mass of stars formed. These values come from the tabulated results of Woosley & Heger (2007) and for the Chabrier IMF (see also Section 3.5 of Kim et al. 2014). Inserting these values into Eq. (5) gives $M_\mathrm{Z} = 0.02896\,\mathrm{M}_\odot$ per one solar mass of stars formed. In other words, in the actual simulation, the amount of metal mass injected into the i-th gas particle is computed as

$$\Delta A_\mathrm{i} = \frac{m_i W(|\boldsymbol{r}_i - \boldsymbol{r}_s|, h_s)}{\sum_{\mathrm{j}=1}^{\mathrm{N}} m_j W(|\boldsymbol{r}_j - \boldsymbol{r}_s|, h_s)}\, A, \tag{6}$$

where A is taken as $\mathcal{Y}'_\mathrm{Z}\Delta\tilde{m}_*$ in this case, $\mathcal{Y}'_\mathrm{Z} = 0.02896$ is the effective yield, $\Delta\tilde{m}_*$ is the mass of the star particle which provides the metal and dust to the i-th gas particle with mass m_i, W is a kernel function, $\boldsymbol{r}_i$ is the positional vector of i-th gas particle measured from the star particle of concern at $\boldsymbol{r}_\boldsymbol{s}$, and h_s is the smoothing length recomputed for the star particle using neighbouring gas particles, respectively.

The produced metals are distributed by the SN shock wave to the neighbouring gas particles within R_sh. If there is only one neighbouring gas particle within R_sh (which could happen in a low resolution simulation), then all the metals are given to the corresponding gas particle.

When a star particle with mass m_* explodes, the following energy E_SN is released (Kim et al. 2014):

$$E_\mathrm{SN} = 0.011 \times 10^{51}\,(m_*/\mathrm{M}_\odot)\ \ \mathrm{erg}\,. \tag{7}$$

As for the kinetic SN feedback, we take 28.3% of the total SN energy ($E_\mathrm{SN,k} = 0.283 E_\mathrm{SN}$; Durier & Dalla Vecchia 2012) as the available kinetic energy, and give the corresponding momentum to gas particles within R_sh in random directions. The remaining 71.7% of the total SN energy is given to the gas as a thermal feedback similarly to the metals above.

2.1.5 *Time evolution of dust abundances*

We solve dust evolution on each gas particle. In this paper, the treatment of grain size distribution is based on the two-size approximation by Hirashita (2015). The whole range of grain radii is represented by large and small grain populations considering that various grain processing mechanisms work differently between these two grain populations. The boundary of these two populations is chosen at $a \simeq 0.03\ \mu$m (Hirashita 2015) based on the full treatment of grain size distribution by Asano et al. (2013b). We adopt typical radii of the large and small grain populations as 0.1 μm and $5 \times 10^{-3}\ \mu$m, respectively. The abundances of the two dust populations on a gas particle are represented by the dust-to-gas mass ratios, $\mathcal{D}_\mathrm{L}$ and $\mathcal{D}_\mathrm{S}$ as

$$\mathcal{D}_\mathrm{L} = \frac{m_\mathrm{L}}{m_\mathrm{g}}, \tag{8}$$

$$\mathcal{D}_\mathrm{S} = \frac{m_\mathrm{S}}{m_\mathrm{g}}, \tag{9}$$

where m_g is the mass of the gas particle, and m_L and m_S are the total mass of large and small grains in the gas particle, respectively. Hereafter we refer to $\mathcal{D}_\mathrm{L}$ ($\mathcal{D}_\mathrm{S}$) as the large (small) grain abundance. The total dust-to-gas ratio $\mathcal{D}_\mathrm{tot}$ is defined as

$$\mathcal{D}_\mathrm{tot} \equiv \mathcal{D}_\mathrm{L} + \mathcal{D}_\mathrm{S}\,. \tag{10}$$

In our simulation, each gas particle has its own dust abundance $\mathcal{D}_{\mathrm{L}(i)}$ and $\mathcal{D}_{\mathrm{S}(i)}$, where suffix i indicates the label for the gas particle. The dust production and destruction processes are calculated for each particle by the model described below.

Based on the two-size model, we calculate the formation and destruction of large and small dust grains on each gas particle using variables and outputs in the simulation. Considering the relevant processes for large and small grains, the equations governing the masses of large and small grains are written as (Hirashita 2015)

$$\frac{\mathrm{d}m_\mathrm{S}}{\mathrm{d}t} = -\mathcal{D}_\mathrm{S}\psi - \frac{m_\mathrm{S}}{\tau_\mathrm{SN}} + \frac{m_\mathrm{L}}{\tau_\mathrm{sh}} - \frac{m_\mathrm{S}}{\tau_\mathrm{co}} + \frac{m_\mathrm{S}}{\tau_\mathrm{acc}}, \tag{11}$$

$$\frac{\mathrm{d}m_\mathrm{L}}{\mathrm{d}t} = -\mathcal{D}_\mathrm{L}\psi + f_\mathrm{in} E_Z - \frac{m_\mathrm{L}}{\tau_\mathrm{SN}} - \frac{m_\mathrm{L}}{\tau_\mathrm{sh}} + \frac{m_\mathrm{S}}{\tau_\mathrm{co}}, \tag{12}$$

where ψ is the star formation rate, E_Z is the injection rate of metals from stars, and f_in is the dust condensation efficiency of the metals in the stellar ejecta. The time-scales of various processes are also introduced: τ_SN is the time-scale of dust destruction by SN shocks, and τ_sh, τ_co, and τ_acc are the time-scales of shattering, coagulation, and accretion, respectively.

Based on the above equations, we formulate the time evolution of the large and small grain abundances in the i-th particle from time t to the next time step $t + \Delta t$ as (see also equation 15 and 16 in Hirashita (2015))

$$\begin{aligned}\mathcal{D}_{\mathrm{L}(i)}(t+\Delta t) &= \mathcal{D}_{\mathrm{L}(i)}(t) - \Delta\mathcal{D}_{(\mathrm{SNe/L})(i)} \\ &\quad - \left(\frac{\mathcal{D}_{\mathrm{L}(i)}(t)}{\tau_\mathrm{sh}} - \frac{\mathcal{D}_{\mathrm{S}(i)}(t)}{\tau_\mathrm{co}}\right)\Delta t \\ &\quad + f_\mathrm{in}\frac{\Delta\tilde{m}_\mathrm{Z}}{m_\mathrm{g}}(1-\delta)\,,\end{aligned} \tag{13}$$

$$\begin{aligned}\mathcal{D}_{\mathrm{S}(i)}(t+\Delta t) &= \mathcal{D}_{\mathrm{S}(i)}(t) - \Delta\mathcal{D}_{(\mathrm{SNe/S})(i)} \\ &\quad + \left(\frac{\mathcal{D}_{\mathrm{L}(i)}(t)}{\tau_\mathrm{sh}} - \frac{\mathcal{D}_{\mathrm{S}(i)}(t)}{\tau_\mathrm{co}} + \frac{\mathcal{D}_{\mathrm{S}(i)}(t)}{\tau_\mathrm{acc}}\right)\Delta t\,,\end{aligned} \tag{14}$$

where $\Delta\mathcal{D}_{(\mathrm{SNe/L})(i)}$ and $\Delta\mathcal{D}_{(\mathrm{SNe/S})(i)}$ are the decrease of the large and small grain abundances in the i-th particle by SN destruction, respectively. The amount of newly produced metals, $\Delta\tilde{m}_Z$, is computed according to Eq. (6). The destroyed fraction of the newly supplied dust from stars, δ, is derived in Appendix A. We explain how to estimate $\Delta\mathcal{D}_{(\mathrm{SNe/L})(i)}$, $\Delta\mathcal{D}_{(\mathrm{SNe/S})(i)}$, τ_sh, τ_co and τ_acc in the following subsections.

One can see in equations (13) and (14) that following processes are implemented in our model: stars produce only large grains; shattering reduces large grains and increases small grains; coagulation reduces small grains and increases large grains; accretion increases only small grains; and SN shocks destroys both large and small grains. As we describe further in the following subsections, accretion and coagulation occurs only in dense ISM, and shattering occurs only in lower density ISM. Accretion is the only process that genuinely increases the dust amount, and shattering and coag-

ulation does not change the total mass of dust. One further important point in our formulation is that 'astration', i.e., the consumption of dust (as well as gas and metals) by star formation is automatically taken care of in our computation, as our dust formulation is using dust-to-gas ratio instead of dust mass itself. If the amount of gas is reduced by star formation, the amount of dust on the relevant gas particle is also reduced by the same factor. The dust in stars are assumed to be locked and do not change as a function of time after the formation of star particles.

The current setup of the code does not allow us to treat delayed dust input from AGB stars. However, contribution from AGB stars can be effectively included in $f_{\rm in}$, although AGB star dust production occurs at the same time as SN dust production in our treatment. As compiled by Inoue (2011b) and Kuo et al. (2013), the value of $f_{\rm in}$ is in the range of $\sim 0.01-0.5$, and it varies among theoretical models adopted. Since implementing delayed metal input requires a deeper modification of the code, we only vary $f_{\rm in}$ to examine the effect of dust production by stars, given that the uncertainty in $f_{\rm in}$ is large. Moreover, as shown later, interstellar processing, especially dust mass growth by accretion, is much more efficient than stellar dust input at ages $\gtrsim$ several hundreds Myr, when AGB stars would start to contribute (Valiante et al. 2009). We leave delayed dust input from AGB stars to future work.

2.2 Dust destruction in SN shocks

Each SN destroys the dust in its sweeping radius. Since each SN is not spatially resolved in our simulations, we simply adopt the following analytic formula for swept gas mass $m_{\rm sw}$ from McKee (1989):

$$m_{\rm sw} = 6800 M_\odot \left(\frac{E_{\rm SN}^{(1)}}{10^{51}\ {\rm erg}}\right)\left(\frac{v_{\rm s}}{100\ {\rm km\ s^{-1}}}\right)^{-2}, \quad (15)$$

where $E_{\rm SN}^{(1)}$ is the energy of a single SN (we fix it to $E_{\rm SN}^{(1)} = 10^{51}$ erg). The shock velocity $v_{\rm s}$ is adopted from McKee et al. (1987), which is based on the Sedov-Taylor solution for single SNe:

$$v_{\rm s} = 200\left(n_0/1\ {\rm cm^{-3}}\right)^{1/7}\left(E_{\rm SN}^{(1)}/10^{51}\ {\rm erg}\right)^{1/14}\ {\rm km\ s^{-1}}, \quad (16)$$

where n_0 is the number density of ambient gas.

A single SN destroys the dust in each gas particle by the following fraction:

$$\eta = \begin{cases} \varepsilon_{\rm SN}\left(\dfrac{m_{\rm sw}}{m_{\rm g}}\right) & (m_{\rm sw} < m_{\rm g}), \\ \varepsilon_{\rm SN} & (m_{\rm sw} \geq m_{\rm g}), \end{cases} \quad (17)$$

where $\varepsilon_{\rm SN}$ is the efficiency of dust destruction in an SN blast wave. We adopt $\varepsilon_{\rm SN} = 0.1$ based on Nozawa et al. (2006) and McKee (1989) unless otherwise stated (see also Jones et al. 1994, 1996).

We estimate the number of SNe affecting the i-th particle, N_i, as

$$N_i = {\rm floor}\left(\frac{E_{\rm SN}}{E_{\rm SN}^{(1)}} W\left(|\boldsymbol{r}_i|, h_*^{\rm exp}\right)\right), \quad (18)$$

where ${\rm floor}(x)$ is Gauss' floor function which returns the integer part of the argument, and $E_{\rm SN}/E_{\rm SN}^{(1)}$ is the number of SN explosions. Since the survival fraction of the dust is $1-\eta$ after an SN, the reduction of dust abundance after N SNe can be estimated as

$$\Delta\mathcal{D}_{({\rm SNe/L,S})(i)}(t) = \left[1-(1-\eta)^N\right]\mathcal{D}_{({\rm SNe/L,S})(i)}(t), \quad (19)$$

which is used in equations (13) and (14).

2.3 Subgrid models for dust physics

Accretion and coagulation of dust occur in dense molecular clouds (Hirashita & Voshchinnikov 2014), which cannot be fully resolved by our current SPH simulations. Therefore, we have to treat these processes by sub-grid models as we describe below.

We impose following criteria for the selection of gas particles hosting unresolved dense gas:

$$n_{\rm gas} > 10\ {\rm cm^{-3}} \quad \text{and} \quad T_{\rm gas} < 10^3\ {\rm K}. \quad (20)$$

We call these gas particles *dense gas particles*, and they occupy lower right corner of the phase diagram shown in Fig. 2. We also assume that the fraction $f_{\rm dense}$ of each dense gas particle is dense enough to allow accretion and coagulation, and that the hydrogen number density and temperature of such dense media are 10^3 cm^{-3} and 50 K, respectively. We adopt $f_{\rm dense} = 0.5$ as a fiducial value, and examine the effect of varying $f_{\rm dense}$ in Section 4.4.4.

2.3.1 *Accretion*

Accretion is a process in which small grains gain their mass by accreting gas from ambient medium. We obtain the time-scale of accretion from eq. (23) in Hirashita & Kuo (2011):

$$\tau_{\rm acc} = \begin{cases} 1.2\times10^6\ {\rm yr}\left(\dfrac{Z}{Z_\odot}\right)^{-1}\left(1-\dfrac{\mathcal{D}_{\rm tot}}{Z}\right)^{-1}/f_{\rm dense} \\ \qquad\qquad ({\rm for}\ \textit{dense gas particles}), \\ \infty\ ({\rm otherwise}). \end{cases} \quad (21)$$

In deriving this equation, we adopted hydrogen number density $n_{\rm H} = 10^3$ cm^{-3}, gas temperature $T_{\rm gas} = 50$ K, sticking efficiency of gas-phase metals $S = 0.3$, and typical radius of small grains $a = 5\times10^{-3}$ μm. The infinity for τ means that we turn off the process. The term $(1-\mathcal{D}_{\rm tot}/Z)^{-1}$ expresses the fact that only the metals in the gas phase contribute to dust growth. We note that the above time-scale is one third of that in Kuo & Hirashita (2012), who treated the time-scale in terms of grain radius, while we define the time-scale by mass growth rate.

2.3.2 *Coagulation*

Coagulation is a process in which small grains collide with each other and turns into large grains. Since it is a collisional process between dust grains, its time-scale $\tau_{\rm co}$ can be estimated based on the collision time-scale (see Appendix B):

$$\tau_{\rm co} = \begin{cases} 2.71\times10^5\ {\rm yr}\left(\dfrac{\mathcal{D}_{\rm S}}{0.01}\right)^{-1}\left(\dfrac{v_{\rm co}}{0.1\ {\rm km\ s^{-1}}}\right)^{-1}/f_{\rm dense} \\ \qquad\qquad ({\rm for}\ \textit{dense clouds}), \\ \infty\ ({\rm for\ others}). \end{cases} \quad (22)$$

In using equation (B4), we adopted $\mathcal{D} = \mathcal{D}_{\rm S}$, $a = 5{\times}10^{-3}$ μm for the typical radius of small grains, $s = 3$ g cm^{-3} for the grain material density, and $v = v_{\rm co}$ for the typical velocity dispersion of small grains. We adopt $v_{\rm co} = 0.1$ km s^{-1} for the fiducial run. Here the typical velocity dispersion is based on the turbulence-induced grain velocity dispersion calculated by a magnetohydrodynamic turbulence model in cold dense molecular clouds (Yan et al. 2004). Since the uncertainty in the velocity dispersion is large, we also examine the case for $v_{\rm co} = 0.01$ km s^{-1} in Section 4.

2.4 Shattering

Shattering is a process in which large grains collide with each other and get shattered into small grains. Since shattering occurs in the diffuse ISM (Hirashita & Yan 2009), it can be spatially resolved in our simulations, and no subgrid model is necessary. We assume that shattering occurs only in gas particles whose gas density is lower than the shattering threshold density $n_{\rm th}^{\rm SH}$. We estimate the shattering time-scale based on the collisional time-scale in Appendix B using directly the gas density of gas particles as

$$\tau_{\rm sh} = \begin{cases} 5.41\times10^7 \ {\rm yr} \left(\dfrac{\mathcal{D}_{\rm L}}{0.01}\right)^{-1} \left(\dfrac{n_{\rm gas}}{1 \ {\rm cm}^{-3}}\right)^{-1} \\ \qquad\qquad (n_{\rm gas} < n_{\rm th}^{\rm SH}) \ , \\ \infty \ (n_{\rm gas} \geq 1 \ {\rm cm}^{-3}) \ . \end{cases} \tag{23}$$

In estimating equation (23), we adopted $a = 0.1$ μm, $s = 3$ g cm^{-3}, $v = 10$ km s^{-1} (a typical velocity dispersion of large grains; Yan et al. 2004), $\mathcal{D} = \mathcal{D}_{\rm L}$, and $n_{\rm H} = n_{\rm gas}$. We adopt $n_{\rm th}^{\rm SH} = 1$ cm^{-3} unless otherwise stated.

3 RESULTS

3.1 Dust enrichment

One of the most fundamental features in our calculation is the spatial distribution of dust in a galaxy. We present the time evolution of surface densities of large and small grains at $t = 0.1$, 0.3, 1, and 5 Gyr in Fig. 3.

At $t \simeq 0.1$ Gyr, the dust-abundant region is limited to the central region of the galaxy because of the relatively high star formation rate (i.e., high dust formation by stellar sources). The processes of increasing the small grain abundance (shattering and accretion) are not efficient yet because of low dust abundance. Thus, the amount of small grains is much smaller than that of large grains in the early phase of evolution.

At $t \simeq 0.3$ Gyr, the distribution of large grains becomes more similar to the gas distribution as the dust enrichment becomes more prevalent in the entire disc. As time passes, the existence of small grains becomes clearer and clearer because large grains are converted to small ones via shattering. After $t \simeq 1.0$ Gyr, accretion becomes dominant (Section 4.2) and the small grain abundance becomes comparable to the large grain abundance in the inner region of the galaxy. This is because the high-density environment in the central part raises both accretion and shattering efficiencies.

At $t \simeq 5.0$ Gyr, not only large grains but also small grains exist in a wide area of several kpc from the galactic centre, tracing the gas distribution well. The density contrast becomes higher than that at $t = 0.1$ Gyr because of the non-linear dependence of accretion on density. In addition, large grains are formed not only via stellar production but also via coagulation in this phase, because the coagulation rate becomes sufficiently high as the small grain abundance increases at later times (Section 4.2).

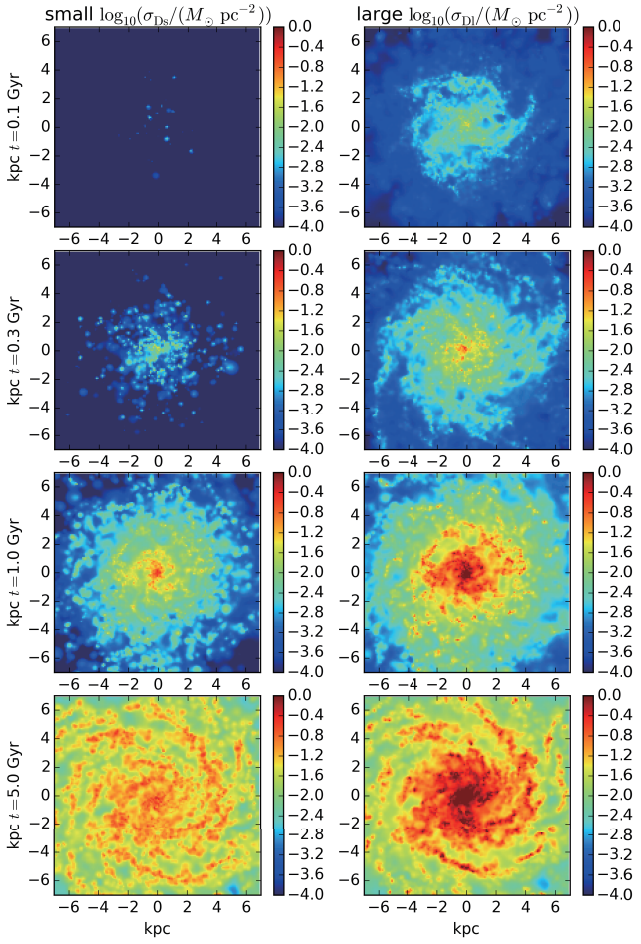

Figure 3. Face-on view of the surface densities of small grains (left column) and large grains (right column) at $t = 0.1, 0.3, 1,$ and 5 Gyr (*top to bottom*).

3.2 Comparison between large and small grain abundances

We have newly incorporated the two-size approximation, which provides information on grain size distribution. Thus, we are able to show the spatially resolved grain size distribution map in a galaxy for the first time, although the grain size distribution is represented by two sizes to save the computational time. In Fig. 4, we present the surface density ratio of small to large grains, $\log_{10}(\mathcal{D}_{\rm S}/\mathcal{D}_{\rm L})$. In the early stage at $t = 0.1$ Gyr, as discussed in Section 3.1, the abundance of large grains is dominant over that of small grains (i.e. most of the area is covered by blue or green colours) in almost all regions of the galaxy, because the dust production is dominated by stellar sources and $\mathcal{D}_{\rm L}$ is large.

By comparing $\mathcal{D}_{\rm S}/\mathcal{D}_{\rm L}$ at various ages in Fig. 4, we find a drastic increase of small grain abundance between $t = 0.1$ and 0.3 Gyr, as we already noted in Section 3.1. Before $t = 0.1$ Gyr, because the shattering time-scale is much shorter than that of accretion, small grains are generated predominantly by shattering. After that, accretion is the dominant process for increasing small grain abundance (Section 4.2). Because accretion is more efficient in more metal-rich and denser gas, we find more regions with a high $\mathcal{D}_{\rm S}/\mathcal{D}_{\rm L}$ close to the central part than in the outskirts at $t \lesssim 0.3$ Gyr. But in some localised dense regions, $\mathcal{D}_{\rm S}/\mathcal{D}_{\rm L}$ is already reaching close to unity, as seen by red spots of actively star-forming regions.

At $t \simeq 1$ Gyr, shattering and coagulation start to show overall balance, and $\mathcal{D}_{\rm S}/\mathcal{D}_{\rm L}$ begin to reach a temporary convergence, and more wider regions start to show redder colour approaching unity, with weaker dependence on the density.

After $t \simeq 5$ Gyr, $\mathcal{D}_{\rm S}/\mathcal{D}_{\rm L}$ reaches close to unity, and the outer part of galaxy also becomes largely red colour. In contrast, we observe a suppression of small grain abundance in the central part (green colour with $\mathcal{D}_{\rm S}/\mathcal{D}_{\rm L} \simeq 0.1$) because of enhanced coagulation there.

4 DISCUSSION

4.1 Time evolution of total mass of each component

We discuss the dust mass budget in the entire galaxy. In Fig. 5, we show the time evolution of the total masses of small and large grains. We also present the total dust and metal masses (metals include both gas-phase and dust-phase components). Because we assume that only large grains are created by stellar sources and adopt a fixed dust condensation efficiency $f_{\rm in}$, the mass ratio of large grains to metals is approximately $f_{\rm in}(= 0.1)$ in the early phase of the evolution. In addition, the abundance of small grains is much smaller in the early epoch such as $\lesssim 0.1$ Gyr. This is because the small grains are created only via shattering and its time scale is much longer than the age.

After $t \sim 0.1$ Gyr, small grains start to increase dramatically by shattering and accretion. However the site where shattering and accretion occur efficiently is limited to the central part (Fig. 3) and the total abundance of dust is still much lower than that of metals. At $\gtrsim 1$ Gyr, because small grains increase further by accretion, a significant fraction of metals is locked into the dust. The total mass ratio of small to large grains is (0.0036, 0.0659, 0.1795, 0.5641), and the total mass ratio of dust to metal is (0.0844, 0.1008, 0.3130, 0.6875) for $t = (0.1, 0.3, 1.0, 5.0)$ Gyr, respectively.

4.2 Contribution of each process

In this section, we examine the contribution of each physical process to dust production and destruction rate. In this calculation, we take into account all gas particles in the simulation, and sum up the contribution of each term on the right-hand-side of Eq. (13) and (14) for each process, as shown in Fig. 6.

Stellar dust production is the dominant production mechanism of large grains in the early stage ($t \lesssim 0.3$ Gyr). For SN dust destruction, we separate the destruction of newly formed dust ($f_{\rm in}\frac{\Delta \tilde{m}_{\rm Z}}{m_{\rm g}}\delta$ in eq. 13) and pre-existing dust (eq. 19) according to the formulation in equation (13) and Appendix A. By construction of our model, the destruction rate of newly formed large grains (SN-destr-2 in Fig. 6) is proportional to the stellar dust production rate (red solid line in Fig. 6). Among all dust processing mechanisms, at $t < 0.1$ Gyr, SN dust destruction of newly formed ones is the most dominant (SN-destr-2 in Fig. 6).

On the other hand, the destruction rate of pre-existing large grains (i.e., SN-destr-1 in Fig. 6 and eq. 19) increases as the system is enriched with dust, simply because the destruction rate is proportional to the destroyed material. The SN destruction rate of small grains also traces the increase of small grains. There is no destruction of small newly formed grains, since we assume that all grains formed by stellar sources are large.

The initial increase of small grains is governed by shattering at $t \lesssim 0.1$ Gyr. As the metallicity and dust abundance increase, accretion catches up with the contribution from shattering, becoming the dominant source of small grains around $t \sim 0.1$ Gyr. As the small grain abundance increases further, the coagulation rate becomes comparable to the stellar dust production rate, which means that coagulation is the most dominant mechanism of producing large grains. Thus, the combination of accretion and coagulation is important in increasing the dust abundance at $t \gtrsim 0.3$ Gyr (note that for the dust mass increase, accretion is more fundamental than coagulation since coagulation itself does not increase the total dust mass). Accretion saturates afterwards because a significant fraction of metals are already accreted on the dust. The contributions of coagulation and shattering become comparable at $t \gtrsim 1$ Gyr; thus, the small-to-large grain abundance ratio is determined by the balance between shattering and coagulation. Note that, since these two processes do not change the total dust amount, the total dust amount is still determined by the balance between accretion and SN destruction. The above evolutionary behaviours of various processes are consistent with those in one-zone calculations (Asano et al. 2013b; Hirashita 2015).

4.3 Dust abundance as a function of metallicity

We plot the time evolution of the relation between dust-to-gas ratio ($\mathcal{D}_{\rm tot}$) and metallicity (Z) for all gas particles in Fig. 7. In this figure, we also plot the relation predicted by the one-zone two-size approximation calculation by Hirashita (2015) (white thin solid line). For the one-zone result, we choose their simple fiducial parameters for various processes as a reference, although in our simulations, the time-scale of each process varies from particle to particle. We also show a simple constant dust-to-metal ratio expected from pure stellar dust production $\mathcal{D}_{\rm tot} = f_{\rm in}Z$ (yellow dashed line) and the saturation limit $\mathcal{D}_{\rm tot} = Z$ (red dot-dashed line).

One can see that a fixed dust-to-metal ratio is a good approximation in the early phase ($t \lesssim 0.1$ Gyr), since the dust evolution is driven by stellar production. Many simulations simply assume a constant dust-to-metal ratio, instead of solving the evolution dust-to-gas ratio (e.g., Yajima et al. 2015). However, because accretion, whose efficiency responds

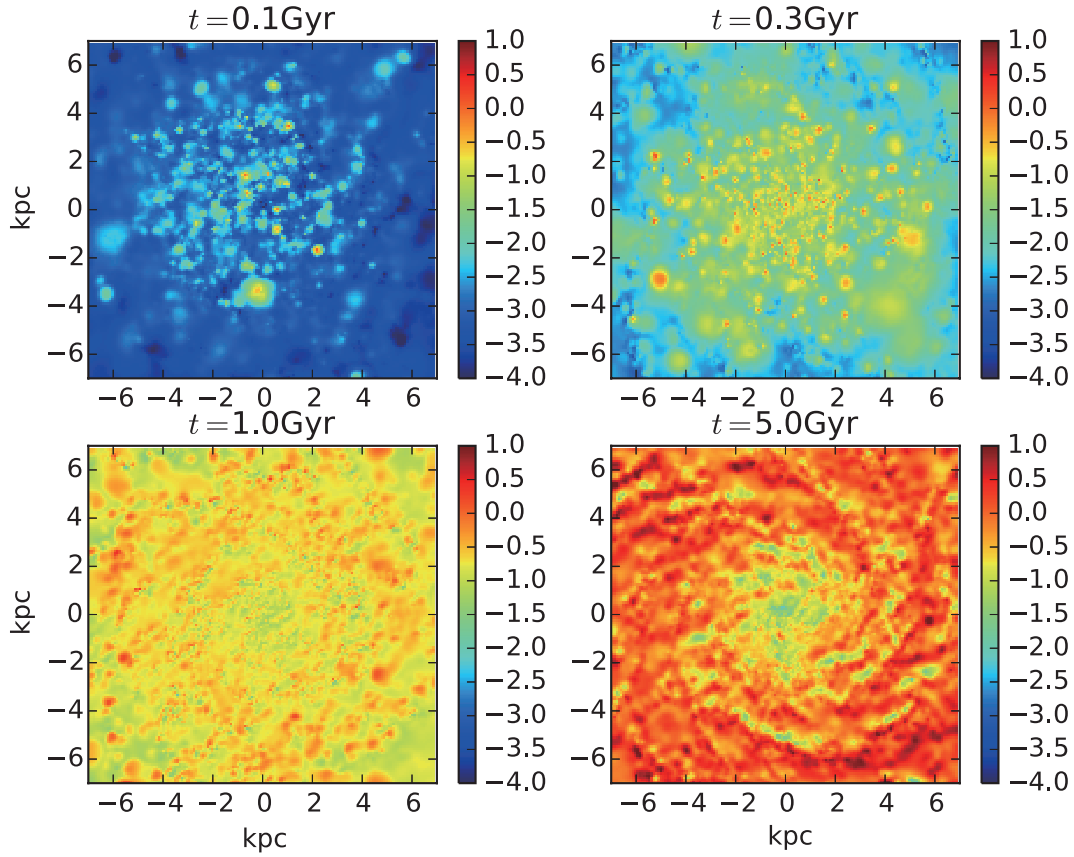

Figure 4. Time evolution of $\log_{10}(\mathcal{D}_{\rm S}/\mathcal{D}_{\rm L})$ at $t = 0.1, 0.3, 1$ and 5 Gyr. Deep blue colour is used for $\mathcal{D}_{\rm S} \sim 0$, corresponding to -4 dex on the colour bar.

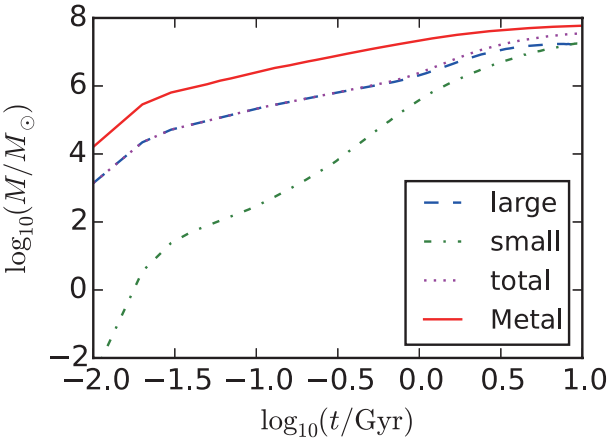

Figure 5. Time evolution of total masses of metals (red solid), total dust mass (dotted), large grains (blue dashed), and small grains (dot-dashed).

to metallicity nonlinearly, is dominating after that, the fixed dust-to-metal ratio no longer gives a good approximation at $t \gtrsim 0.3$ Gyr. The important feature of the increase of dust-to-gas mass ratio due to accretion is that it becomes prominent above a certain metallicity. This metallicity is called *critical metallicity* in, for example, Asano et al. (2013a). This critical behaviour of accretion in terms of metallicity is caused by the metallicity dependence of the accretion efficiency, as is clear from the accretion time-scale in equation (21) (see also Dwek 1998; Zhukovska et al. 2008). As the system is enriched with metals, the $\mathcal{D}_{\rm tot}$–Z relation extends towards higher metallicities and higher $\mathcal{D}_{\rm tot}$. Because accretion saturates after a significant fraction of gas-phase metals are locked into dust, the increase of $\mathcal{D}_{\rm tot}$ as a function of Z becomes moderate at the highest metallicity range.

We also plot the observed $\mathcal{D}_{\rm tot}$–Z relation for nearby galaxies with each point corresponding to each individual galaxy (not spatially resolved) (Rémy-Ruyer et al. 2014; Zhukovska 2014). Since our theoretical plots are for each SPH particle in our single-galaxy simulation, strictly speaking, we cannot compare our results with an unresolved nearby galaxy sample. Nevertheless, the fact that our models roughly reproduces the observed $\mathcal{D}_{\rm tot}$–Z relation for nearby galaxies indicates that our implementation of various dust formation and processing mechanisms is successful in catching the trend of dust evolution as a function of metallicity.

In Fig. 8, we also show the relation between small-to-large grain abundance ratio and metallicity, in order to clarify the evolution of grain size distribution. In the earliest stage of evolution the main source of small grains is shattering, whose efficiency increases in proportion to the large grain abundance. While the large grain abundance increases as a function of metallicity by stellar dust production, the production rate of small grains depends on the square of the large grain abundance. Thus $\mathcal{D}_{\rm S}/\mathcal{D}_{\rm L}$ has a positive correlation with Z. At $t \gtrsim 0.3$ Gyr, the $\mathcal{D}_{\rm S}/\mathcal{D}_{\rm L}$ shows a strong

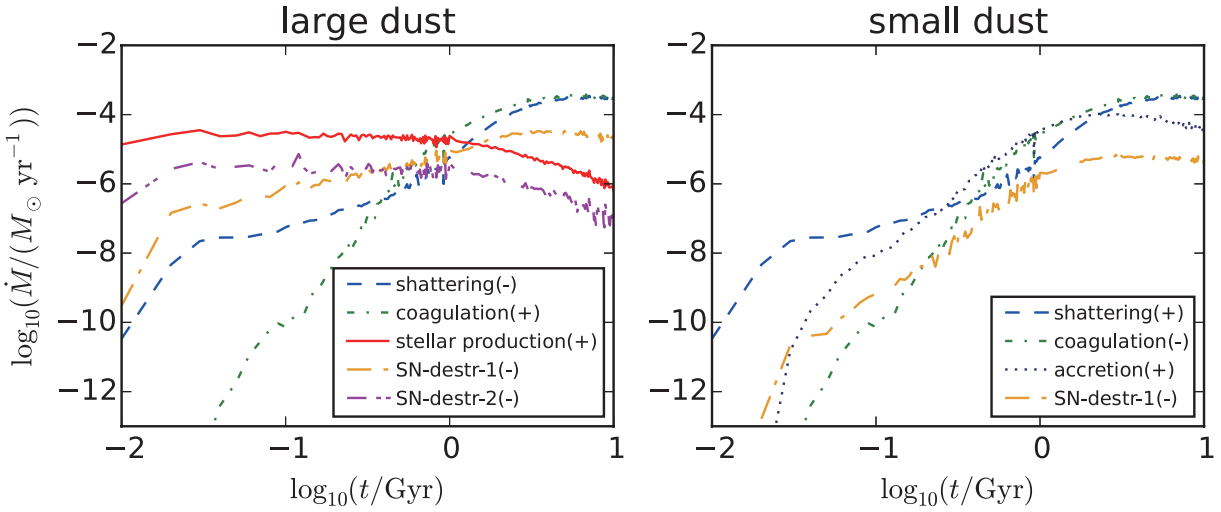

Figure 6. Time evolution of dust production and destruction rate for each process. *Left panel*: the terms from the right-hand-side of equation (13) are shown for large grains: shattering (blue dashed), coagulation (green dot-dashed), stellar production (red solid), SN-destr-1 (orange dot-long-dashed; corresponding to the destruction rate of pre-existing dust in eq. (19)), and SN-destr-2 (purple dot-dot-dashed; corresponding to the destruction rate of newly formed dust, $f_{\rm in}\frac{\Delta\tilde{m}_{\rm Z}}{m_{\rm g}}\delta$). *Right panel*: the terms from the right-hand-side of equation (14) are shown for small grains: shattering (blue dashed), coagulation (green dot-long-dashed), accretion (black dotted), and SN-destr-1 (orange dot-dashed; same as left panel).

dependence on Z around $Z \sim 0.1\ \mathrm{Z}_\odot$ because of accretion. At higher metallicities, as is clear in the plots at $t = 1$ and 5 Gyr, $\mathcal{D}_{\rm S}/\mathcal{D}_{\rm L}$ decreases as Z increases because small grains turn into large ones via coagulation. The above behavior on the $\mathcal{D}_{\rm S}/\mathcal{D}_{\rm L}$–$Z$ diagram is consistent with the analysis in Hirashita (2015).

At $t = 5$ Gyr, the distribution of $\mathcal{D}_{\rm S}/\mathcal{D}_{\rm L}$ seems to split into two components at $\log_{10}(Z/Z_\odot) \lesssim -0.5$. The upper component with $\mathcal{D}_{\rm S}/\mathcal{D}_{\rm L} \sim 1$ corresponds to low temperature ($T_{\rm gas} < 10^4$ K) and diffuse gas ($10^{-2} \lesssim n_{\rm gas} < 1\ \mathrm{cm}^{-3}$) in the disk, and the bottom component with $\mathcal{D}_{\rm S}/\mathcal{D}_{\rm L} \sim 0.1$ corresponds to high temperature ($T_{\rm gas} > 10^4$ K) and diffuse gas ($n_{\rm gas} < 1\ \mathrm{cm}^{-3}$, but largely $\lesssim 10^{-2}\ \mathrm{cm}^{-3}$; see the phase diagram in Fig. 2) in both disk and circum-galactic regions affected by SN feedback. The former component has higher densities than the latter component; therefore the impact of shattering is much stronger, resulting in higher $\mathcal{D}_{\rm S}/\mathcal{D}_{\rm L}$.

4.4 Parameter dependence

There are some uncertain parameters involved in the above subgrid dust physics models. Although the values of those parameters are chosen based on physical reasoning, it is still worth examining the effect of varying them. Below we examine how a representative parameter for each process affects the results. We use the $\mathcal{D}_{\rm tot}$–Z and $\mathcal{D}_{\rm S}/\mathcal{D}_{\rm L}$–$Z$ diagrams to examine the effects of various processes, since we have shown above that these diagrams are useful for such a purpose. We find that the qualitative behaviour as a function of time in this diagram does not change so much when we vary the parameters, therefore we focus on $t = 1$ Gyr for this comparison.

4.4.1 *Stellar dust production $f_{\rm in}$*

For stellar dust production, the condensation efficiency $f_{\rm in}$ is the key parameter. Inoue (2011a) and Kuo & Hirashita (2012) found that $f_{\rm in}$ varies in the range of 0.01–0.5 even among different theoretical calculations.

To clarify the effect of varying $f_{\rm in}$, we compare the results of $f_{\rm in} = 0.01$ and our fiducial value $f_{\rm in} = 0.1$ in Fig. 9. The dust-to-gas ratio at low metallicity is simply proportional to $f_{\rm in}$ (i.e., $\mathcal{D}_{\rm tot} \sim \mathcal{D}_{\rm L} \sim f_{\rm in}Z$), because stellar dust production dominates the dust abundance increase. The value of $\mathcal{D}_{\rm S}/\mathcal{D}_{\rm L}$ at low metallicity is also lower for $f_{\rm in} = 0.01$ than for $f_{\rm in} = 0.1$, because the production rate of small grains by shattering is proportional to $\mathcal{D}_{\rm L}$ according to equation (23).

However, both $\mathcal{D}_{\rm tot}$ and $\mathcal{D}_{\rm S}/\mathcal{D}_{\rm L}$ reach similar values at high metallicity regardless of the difference in $f_{\rm in}$, because the processes other than stellar dust production, especially accretion, dominate these quantities. Thus changing $f_{\rm in}$ affects the dust abundance only at low metallicities, typically $Z \lesssim 0.1\ \mathrm{Z}_\odot$.

4.4.2 *Density threshold of shattering*

We also examine the dependence on the treatment of shattering. The strength of shattering is mostly regulated by the density threshold below which shattering occurs ($n_{\rm th}^{\rm SH}$). Examining a low threshold density for shattering is especially important since setting too-high a threshold may cause an unreasonably strong shattering effect, because the shattering time-scale is inversely proportional to the density (equation (23)). In Fig. 10, we compare the results for a lower density threshold $n_{\rm th}^{\rm SH} = 0.1\ \mathrm{cm}^{-3}$ and the fiducial $n_{\rm th}^{\rm SH} = 1\ \mathrm{cm}^{-3}$ (equation 23). Since shattering occurs in lower density gas than $n_{\rm th}^{\rm SH}$, lowering this threshold density reduces the amount of gas which will be affected by shattering.

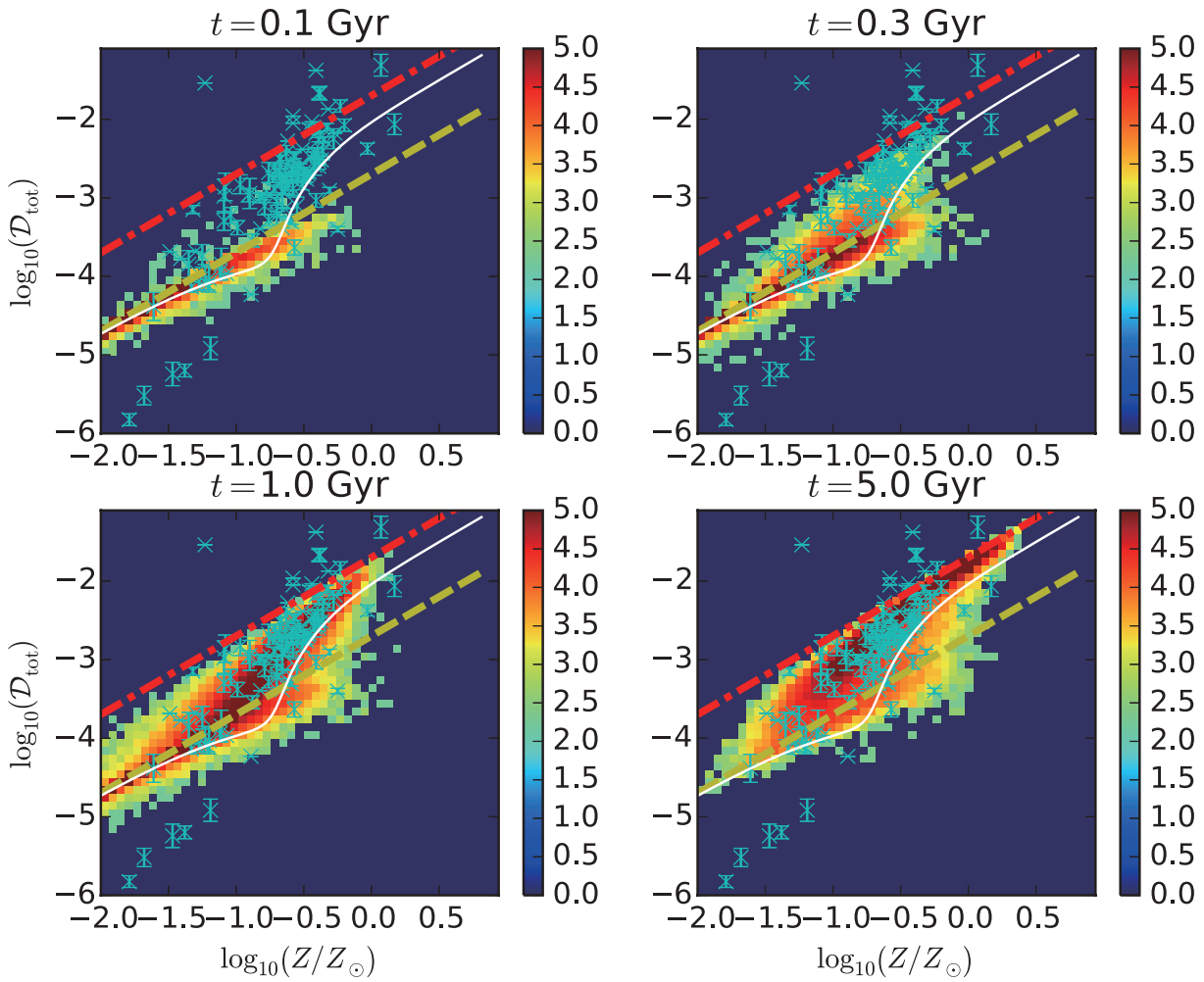

Figure 7. Distribution of gas particles on the $\mathcal{D}_{\rm tot} - Z$ plane at $t = 0.1, 0.3, 1$ and 5 Gyr as labelled. The colour indicates the logarithmic surface density of the gas particle on this diagram. The white line represents the one-zone calculation by Hirashita (2015). The yellow dashed and red dot-dashed lines denote the linear relation of the stellar yield ($\mathcal{D}_{\rm tot} = f_{\rm in} Z$) and the saturation limit ($\mathcal{D}_{\rm tot} = Z$), respectively. Cyan crosses denote the observational data of nearby galaxies taken from Rémy-Ruyer et al. (2014) and Zhukovska (2014).

From this comparison, we find that the increase of $\mathcal{D}_{\rm tot}$ is slightly suppressed at $Z > 0.1 {\rm Z}_\odot$ for a lower $n_{\rm th}^{\rm SH}$, because less production of small grains by shattering leads to less efficient accretion. Suppression of small-grain formation is clearly observed in lower $\mathcal{D}_{\rm S}/\mathcal{D}_{\rm L}$ at low metallicities with lower $n_{\rm th}^{\rm SH}$ in Fig. 10, and the overall distribution of $\mathcal{D}_{\rm S}/\mathcal{D}_{\rm L}$ is also slightly lower even at higher metallicities.

4.4.3 Grain velocity for coagulation

The coagulation time-scale is regulated by the typical velocity of small grains $v_{\rm co}$. As shown by Yan et al. (2004), the velocity of small grains in the dense medium depends strongly on gas density. Our fiducial value ($v_{\rm co} = 0.1$ km s^{-1}) is taken from their calculation for molecular clouds, however, if we adopt their dense cloud cases, the velocity dispersion could be smaller by an order of magnitude. Thus, we examine the case of a smaller $v_{\rm co} = 0.01$ km s^{-1}.

Fig. 11 compares the results with $v_{\rm co} = 0.1$ (fiducial) and 0.01 km s^{-1}. We observe that a larger $v_{\rm co}$ (i.e., more efficient coagulation) predicts a lower $\mathcal{D}_{\rm S}/\mathcal{D}_{\rm L}$ at high metallicities, as the small grains are converted into large grains via coagulation more. The resulting $\mathcal{D}_{\rm S}/\mathcal{D}_{\rm L}$ is roughly inversely proportional to $v_{\rm co}$ at $Z \gtrsim 0.3\,{\rm Z}_\odot$, because it scales with the inverse of coagulation efficiency. Since coagulation conserves the total dust mass, $\mathcal{D}_{\rm tot}$ is hardly affected by the change of $v_{\rm co}$.

4.4.4 Mass fraction of dense cloud: $f_{\rm dense}$

The subgrid parameter introduced to describe accretion and coagulation is the fraction of dense clouds $f_{\rm dense}$ (Section 2.3). In addition to the fiducial case of $f_{\rm dense} = 0.5$, we also examine a low fraction $f_{\rm dense} = 0.1$, as shown in Fig. 12.

The increase of $\mathcal{D}_{\rm tot}$ by accretion occurs at higher metallicity for $f_{\rm dense} = 0.1$ than for $f_{\rm dense} = 0.5$, because of a lower efficiency of accretion. In other words, a higher metallicity is required for accretion to be efficient enough to raise the dust-to-gas ratio. However, the dust-to-gas ratio eventually reaches similar values at solar metallicity in both cases.

The effect of coagulation is seen in $\mathcal{D}_{\rm S}/\mathcal{D}_{\rm L}$, which is systematically lower at high metallicities for $f_{\rm dense} = 0.5$

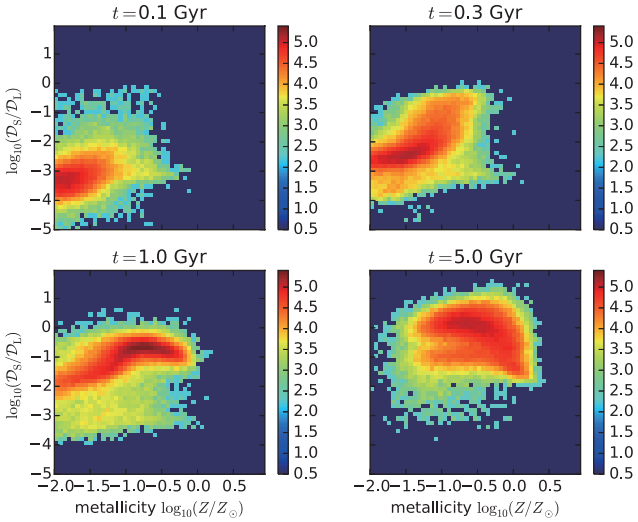

Figure 8. Small-to-large grain abundance ratio ($\mathcal{D}_S/\mathcal{D}_L$) as a function of metallicity Z at various epoch. The colour indicates the logarithmic surface density of the gas particle in each pixel of this diagram.

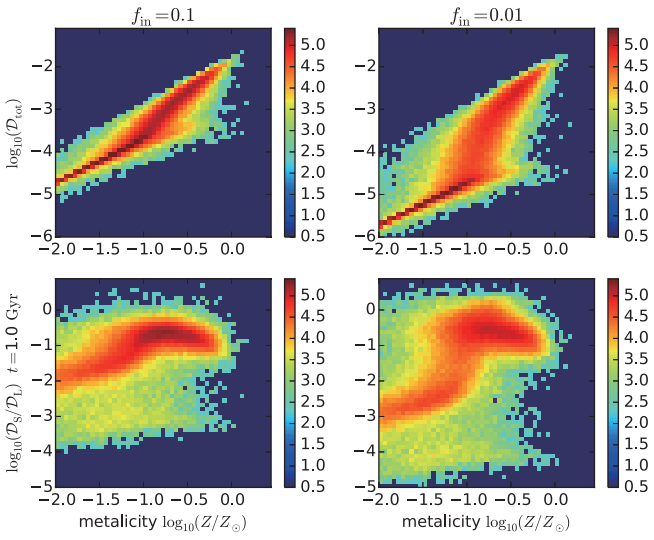

Figure 9. Dependence of $\mathcal{D}_{tot} - Z$ and $\mathcal{D}_S/\mathcal{D}_L - Z$ relations on the dust coagulation efficiency f_{in} at $t = 1$ Gyr. In the left column, we plot the distribution of gas particles for the fiducial case ($f_{in} = 0.1$), which are also shown in Figs. 7 and 8. In the right column, we show the results of $f_{in} = 0.01$ for comparison.

than for $f_{dense} = 0.1$ due to more efficient coagulation. In contrast, the change of f_{dense} does not affect the results at low metallicities, because neither coagulation nor accretion is the dominant mechanism for driving the dust evolution at low metallicities.

4.4.5 Dust destruction efficiency in an SN blast: ε_{SN}

Nozawa et al. (2006) studied the efficiency of dust destruction in an SN blast for various dust species, and showed that it varies by about a factor of four among different dust species. Therefore we also simulate a high efficiency

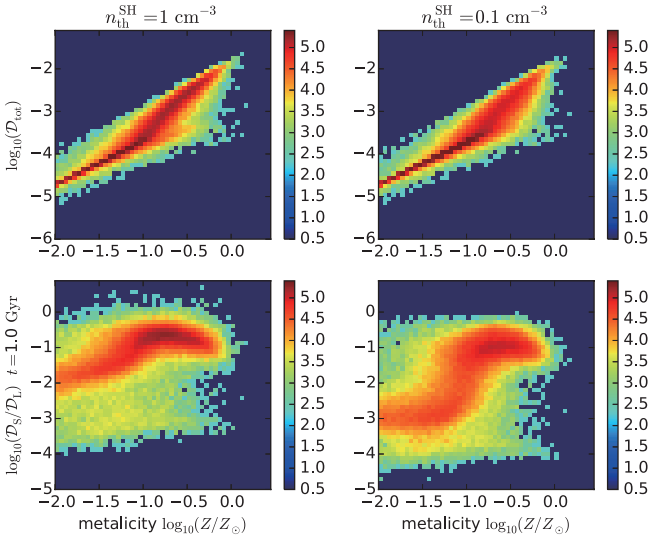

Figure 10. Same as Fig. 9, but for the comparison between $n_{th}^{SH} = 1$ cm^{-3} (left column) and $n_{th}^{SH} = 0.1$ cm^{-3} (right column).

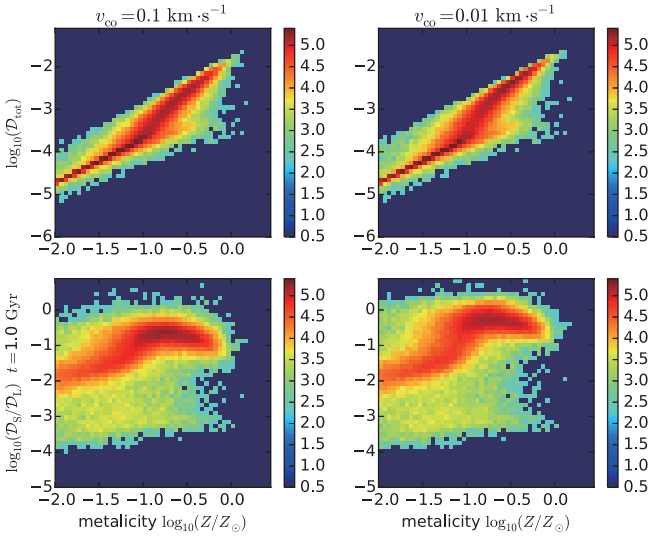

Figure 11. Same as Fig. 9, but for the comparison between $v_{co} = 0.1$ km s^{-1} (left column) and $v_{co} = 0.01$ km s^{-1} (right column).

case with $\varepsilon_{SN} = 0.4$ and compare with the fiducial case, $\varepsilon_{SN} = 0.1$, in Fig. 13.

We find that the dispersion of gas particles on the $\mathcal{D}_{tot} - Z$ plane at $Z \sim 0.1\,Z_\odot$ is greater for $\varepsilon_{SN} = 0.4$ than for $\varepsilon_{SN} = 0.1$. The dispersion is especially increased toward small $\mathcal{D}_{tot}$. In addition, $\mathcal{D}_S/\mathcal{D}_L$ is slightly suppressed at $Z \sim 0.03\,Z_\odot$ for $\varepsilon_{SN} = 0.4$ case compared to $\varepsilon_{SN} = 0.1$ case. These results suggest that the location of the increase of $\mathcal{D}_{tot}$ and $\mathcal{D}_S/\mathcal{D}_L$ by accretion is shifted to higher metallicity if SN destruction is stronger. This is consistent with the one-zone calculation result in Hirashita (2015). The 'disturbance' by SN destruction also increases scatter at high metallicities. Therefore, although SN destruction does not change the overall behaviour in the $\mathcal{D}_{tot} - Z$ diagram, it

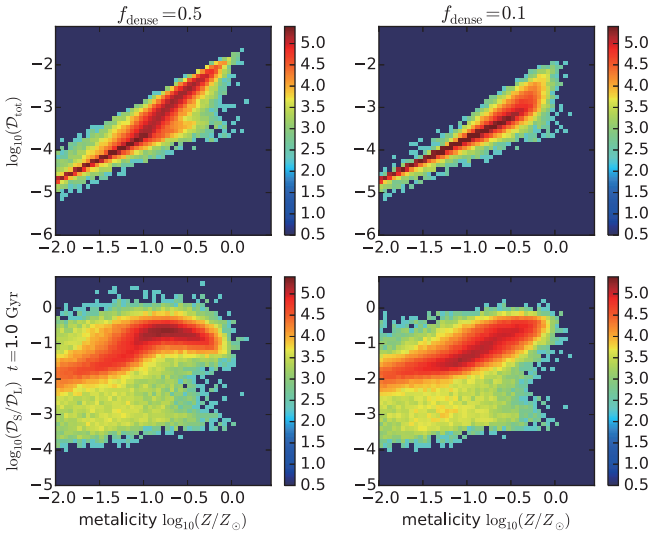

Figure 12. Same as Fig. 9, but for the comparison between $f_{\rm dense} = 0.5$ (left column) and $f_{\rm dense} = 0.1$ (right column).

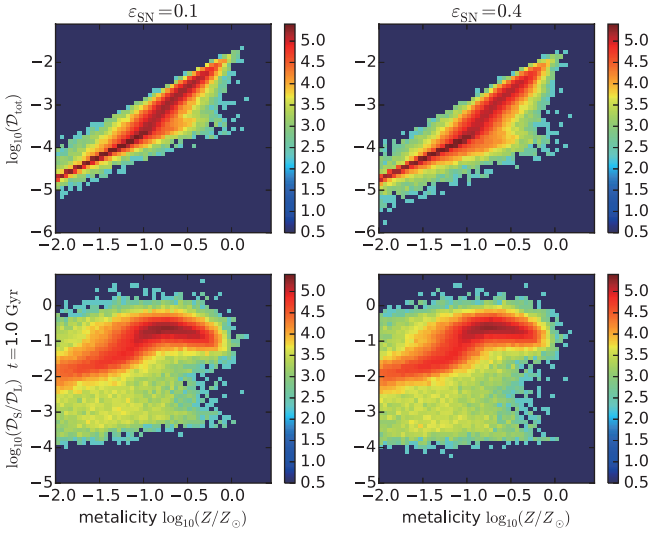

Figure 13. Same as Fig. 9, but for the comparison between $\varepsilon_{\rm SN} = 0.1$ (left column) and $\varepsilon_{\rm SN} = 0.4$ (right column).

produces more scatter in the dust abundance and grain size distribution.

5 OBSERVATIONAL IMPLICATIONS

Although the main purpose of this paper has been to establish a computational framework of dust evolution in galaxy simulations, it is an important step to compare the output of simulations with observational data. Among the quantities that can be compared directly with observations, we choose the radial distribution of dust-to-gas ratio and dust-to-metal ratio. The dust-to-metal ratio is referred to as the 'depletion' in this paper.

Depletion is one of the observational quantities that suggest the existence of dust in the ISM (e.g., Mathis 1990).

Galaxy	m_* [10^9M$_\odot$]	ψ [M$_\odot$/yr]	sSFR [Gyr^{-1}]	Category
HolmbergII	$0.20^{(1)}$	$6.61^{(1)}$	$33.128^{(1)}$	I
NGC925	$7.94^{(1)}$	$10.72^{(1)}$	$1.350^{(1)}$	II
NGC3621	$58.88^{(2)}$	$125.89^{(3)}$	2.138	II
NGC628	$12.59^{(1)}$	$9.77^{(1)}$	$0.776^{(1)}$	III
NGC2403	$2.14^{(4)}$	$1.74^{(4)}$	$0.813^{(4)}$	III
NGC4736	$19.95^{(1)}$	$7.76^{(1)}$	$0.389^{(1)}$	III
NGC5055	$63.10^{(1)}$	$11.75^{(1)}$	$0.186^{(1)}$	III
NGC5194	$39.81^{(1)}$	$7.76^{(1)}$	$0.195^{(1)}$	III
NGC7793	$3.39^{(2)}$	$3.16^{(3)}$	0.933	III
NGC2841	$79.43^{(1)}$	$6.92^{(1)}$	$0.087^{(1)}$	IV
NGC3031	$85.11^{(2)}$	$12.59^{(3)}$	0.148	IV
NGC3198	$10.00^{(4)}$	$1.00^{(4)}$	$0.100^{(4)}$	IV
NGC3351	$56.23^{(4)}$	$3.31^{(4)}$	$0.059^{(4)}$	IV
NGC3521	$190.55^{(4)}$	$10.47^{(4)}$	$0.055^{(4)}$	IV
NGC7331	$79.43^{(1)}$	$9.12^{(1)}$	$0.115^{(1)}$	IV

Table 2. Stellar mass (m_*), global star formation rate (ψ), specific star formation rate (sSFR) and corresponding category of each galaxy. The references of each values are described as a superscript. (1), (2), (3) and (4) correspond to Heesen et al. (2014), Dutta et al. (2013); de Blok et al. (2008) and Zhou et al. (2015), respectively. For SFR and stellar mass, Dutta et al. (2013) and de Blok et al. (2008) are used, respectively.

There is no direct observational data for grain size distributions, although extinction curves and dust emission spectra may give some constraints on them (Yajima et al. 2014; Nozawa et al. 2015; Hou et al. 2016). However, further modelling is necessary to predict dust extinction and emission, requiring additional sets of assumptions (Draine & Li 2001; Li & Draine 2001). Therefore we leave those issues for our future work (Hou et al., in preparation).

5.1 Radial profile

We discuss and compare the total dust surface density in simulations and observations. First, we show the time evolution of the radial profile of dust surface density in Fig. 14. Overall, the dust surface density increases as time passes due to dust enrichment. The dust surface density rapidly increases from $t = 0.3$ Gyr to 1 Gyr due to accretion, especially in the central region. However, the star formation activity in the central region is also high and the gas is consumed rapidly before $t \simeq 1$ Gyr. Thus the dust surface density is saturated by astration (i.e., consumption of gas, metals and dust by star formation) at the central region after $t \simeq 1$ Gyr. In contrast, the dust-to-gas ratio and metallicity monotonically increase at all radii even in this phase, because astration decreases dust, metals and gas at the same rate.

The time evolution of radial profile of $\mathcal{D}_{\rm S}/\mathcal{D}_{\rm L}$ can be understood in the following way. In the early phase such as $t \lesssim 0.3$ Gyr, the source of small grains is mainly shattering and the abundance of small grains is determined only by that of large grains. Hence $\mathcal{D}_{\rm S}/\mathcal{D}_{\rm L}$ roughly follows the radial profile of $\mathcal{D}_{\rm tot}$. At $0.2 \lesssim t \lesssim 0.5$ Gyr, small grains starts to increase more than large grains via accretion, especially in the central region where the gas density (i.e., efficiency of shattering) and star formation rate (i.e., production rate of large grains) are high. The rapid increase in $\mathcal{D}_{\rm S}/\mathcal{D}_{\rm L}$ is observed at later epochs (~ 1 Gyr) in the outer region. In

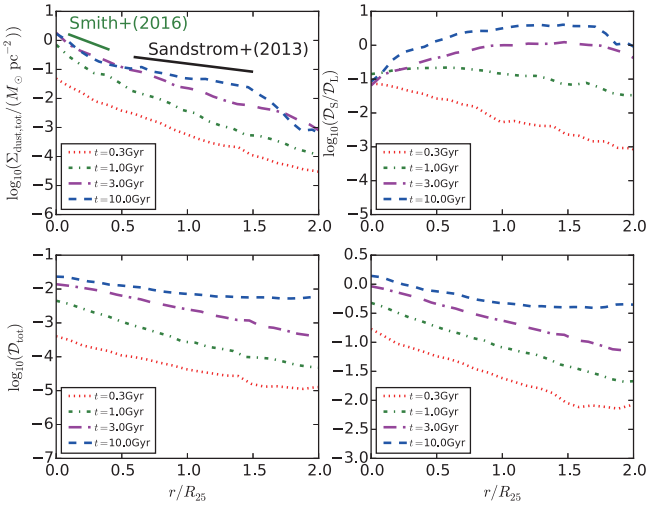

Figure 14. Radial profiles of the dust surface density $\Sigma_{\rm dust,tot}$ (*top-left*), small-to-large grain abundance ratio $\mathcal{D}_{\rm S}/\mathcal{D}_{\rm L}$ (*top-right*), total dust-to-gas mass ratio $\mathcal{D}_{\rm tot}$ (*bottom-left*), and metallicity Z (*bottom-right*) at $t = 0.3$ Gyr (dotted), 1.0 Gyr (dot-short-dashed), 3.0 Gyr (dot-long-dashed), and 10.0 Gyr (dashed). In the top left panel, we also overplot the observationally derived radial profiles by Sandstrom et al. (2013) and Smith et al. (2016).

contrast, in the central region, coagulation decreases $\mathcal{D}_{\rm S}/\mathcal{D}_{\rm L}$ at $t \gtrsim 1$ Gyr.

In the later stage of simulation ($t \gtrsim 1$ Gyr), shattering further increases $\mathcal{D}_{\rm S}/\mathcal{D}_{\rm L}$. The reason is the following. As time passes, dense gas particles are consumed by star formation and the sites of coagulation monotonically decreases. On the other hand, the sites of shattering do not decrease so much, because diffuse ISM does not form stars. As a result, $\mathcal{D}_{\rm S}/\mathcal{D}_{\rm L}$ continues to increase after $t = 1$ Gyr.

The radial profile of dust-to-gas ratio have been observationally investigated by Sandstrom et al. (2013) for nearby galaxies. To cancel the galaxy size effect, we normalise the radius by R_{25} (the radius at which surface brightness falls to 25 mag arcsec^{-2}) for the simulated galaxy, following Mattsson & Andersen (2012). The value of R_{25} changes as time passes, because the distribution of stellar component changes: $R_{25} = (6.9, 7.0, 7.2, 8.4)$ kpc at $t = (0.3, 1.0, 3.0, 10.0)$ Gyr, respectively.

The surface density profile of stellar disc in a spiral galaxy, $\Sigma_*(r)$, can be approximately described by a single exponential function as $\Sigma_*(r) = \Sigma_0 \exp(-r/R_{\rm d})$, where Σ_0 is the central surface density. The scale length of stellar disk, $R_{\rm d}$, is determined by fitting the stellar surface density profile of simulated galaxy at each epoch. We relate $R_{\rm d}$ and R_{25} by $R_{25} \simeq 4R_{\rm d}$ (Elmegreen 1998). This relation can be confirmed by the data in, e.g., de Vaucouleurs & Pence (1978). Sandstrom et al. (2013) showed that the stacked radial profile of dust surface density is well explained by $\exp(-0.56\, r/R_{25})$. We plot this slope in Fig. 14 together with the simulation results, and find that the simulation results at $t > 3.0$ Gyr agree well with the observed one by Sandstrom et al. (2013). Smith et al. (2016) also gave a fit of $-1.7\,{\rm dex}\, R_{25}^{-1}$ to the observed dust surface density profile using 110 spiral galaxies in the Herschel Reference Survey, as shown in the top left panel of Fig. 14.

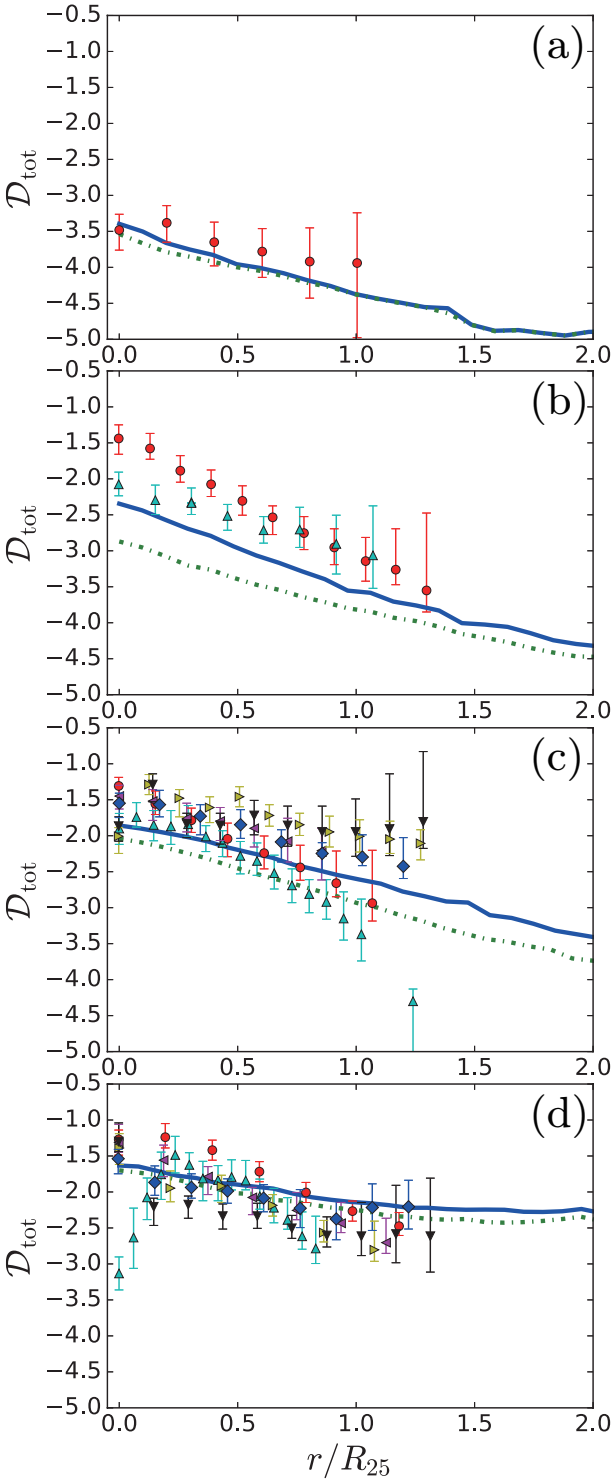

Figure 15. Comparison of the radial profiles of total dust-to-gas ratio with observational data taken from Mattsson & Andersen (2012). We scaled the radius with R_{25}. In panel (*a*), circle points represent the observational radial profile of Holmberg II. In panel (*b*), circle and triangle points show that of NGC 3621 and NGC 925, respectively. In panel (*c*) & (*d*), circle, $\triangle$, $\triangleleft$, $\triangleright$, $\triangledown$, and diamond points are that of NGC 628, NGC 2403, NGC 4736, NGC 5194 and NGC 7793, respectively. The solid and dotted lines represent the case with $f_{\rm dense} = 0.5$ and 0.1, respectively.

In addition, we also compare our simulation against the observed data by Mattsson & Andersen (2012), who investigated the radial profile of dust-to-gas ratio and dust-to-metal ratio in nearby star-forming galaxies (mainly spiral galaxies). They used the metallicity calibration method of Moustakas et al. (2010). In order to compare the simulation snapshots at various ages with observations, we classify the observed galaxy sample according to their evolutionary stage. We use the specific star formation rate (sSFR) as an indicator of evolutionary stage, as the build-up of stellar mass is tightly related to the metal and dust enrichment. We take sSFR in the literature as summarised in Table 2, and divide the sample into following four categories: 10 Gyr^{-1} < sSFR, 1 $\mathrm{Gyr}^{-1} \leq$ sSFR $\leq$ 10 Gyr^{-1}, $10^{-0.8}$ < sSFR < 1 Gyr^{-1}, and sSFR < $10^{-0.8}$ Gyr^{-1} for Category I, II, III and IV, respectively. Holmberg II is a dwarf irregular galaxy, not a spiral galaxy, but it is also included as a representative of young objects, although the comparison should be taken as preliminary until we really simulate a dwarf irregular galaxy. In our simulated galaxy, we adopt the ages 0.3, 1, 3, and 10 Gyr, when the average sSFR is ~ 3 , 1, 0.3, and 0.1 Gyr^{-1}, respectively. We compare the simulation results at $t = 0.3, 1, 3$, and 10 Gyr with Category I, II, III and IV, respectively.

We plot the radial profile of $\mathcal{D}_{\rm tot}$ of each category in Fig. 15. Since the radial profile is sensitive to grain growth, we show the results with $f_{\rm dense} = 0.5$ (solid line) and 0.1 (dotted line). The dust-to-gas ratio in the 'youngest' phase represented by Category I (Holmberg II) is broadly reproduced in terms of not only the slope but also the absolute value. The difference between the results with $f_{\rm dense} = 0.5$ and 0.1 is small, because the dust formation is dominated by stellar production at this early age.

For the galaxies in Category II compared with the simulation result at $t = 1$ Gyr in Fig. 15b, the slope of the radial profile is reproduced well, although the simulated $\mathcal{D}_{\rm tot}$ tend to be lower than the observed data points. However, the dust-to-metal ratio is reproduced well over the entire radii (see Section 5.2); thus, we suspect that the metallicity evolution implemented in our model underproduces the metallicities for those galaxies. It requires a further check in the future, but this could simply be regarded as an early transient feature in isolated galaxy simulations of this type which does not include any cosmological evolution.

The galaxies in Category III are compared with the simulation results at $t = 3.0$ Gyr in Fig. 15c. Although the observed data points have large dispersion, the simulations roughly reproduce both the absolute value and slope of except the outer part of NGC 2403. Even when we adopt the smaller $f_{\rm dense}$, the result changes only by 30 % and the difference is smaller than most observational uncertainties.

The simulation results at $t = 10$ Gyr are compared with the galaxies in Category IV in Fig. 15d. The simulated slope is shallower at $t = 10$ Gyr than at 3.0 Gyr, because the increase of $\mathcal{D}_{\rm tot}$ by accretion is efficient up to the outer radii. The simulation result reproduces the overall trend of observed data except for the central part of NGC 3031. Since the deficiency of dust abundance in NGC 3031 is also seen in the dust-to-metal ratio (see Section 5.2), the dust destruction in the central part of NGC 3031 may be much more efficient than assumed in this paper. Because the accretion is saturated at this late age, the dependence of simulation result on $f_{\rm dense}$ is very weak.

5.2 Depletion

We show the radial profiles of depletion (i.e., dust-to-metal ratio), which is defined as $\mathcal{D}_{\rm tot}/Z$. We compare the simulated radial profile of $\mathcal{D}_{\rm tot}/Z$ in Fig. 16, similarly to Fig. 15. We calculate the depletion at each radius by

$$\frac{\mathcal{D}_{\rm tot}}{Z}(r) \equiv \frac{\sum_i m_i^{\rm gas} \mathcal{D}_{{\rm tot},i}}{\sum_i m_i^{\rm gas} Z_i^{\rm gas}} \ , \tag{24}$$

where the two mass-weighted values $m_i^{\rm gas}\mathcal{D}_{{\rm tot},i}$ and $m_i^{\rm gas} Z_i^{\rm gas}$ are summed up in each ring for all SPH particles in the appropriate radial range. We use 100 bins on the linear scale in $0 \leq r/R_{25} \leq 2$.

We find that the depletion is almost constant in the early phase at $t = 0.3$ Gyr and the models broadly reproduce the observed depletion in Holmberg II (Category I). At this stage, the level of depletion is broadly determined by the condensation efficiency in stellar ejecta. Thus the depletion is almost constant ($\simeq f_{\rm in} = 0.1$). Since accretion is not efficient at this stage, the simulation result is almost independent of $f_{\rm dense}$.

For the galaxies in Category II which are compared with the simulation at $t = 1$ Gyr in Fig. 16b, we find that the depletion profile is broadly consistent with the observational data. As interpreted by Mattsson & Andersen (2012), the decreasing trend of depletion with increasing radius is caused by more efficient accretion in the centre than in the outer regions, since dust growth by accretion is more efficient in more metal-rich environment. When we adopt $f_{\rm dense} = 0.1$, we underestimate the depletion in the central region.

For the galaxies in Category III compared with the simulation at $t = 3$ Gyr in Fig. 16c, the simulation somewhat overpredicts depletion against observed data. The radial gradient of depletion is shallower in Category III than in Category II, because the effect of accretion becomes more prevalent up to larger radii at later times. When we consider the case of $f_{\rm dense} = 0.1$, the discrepancy between the simulation and observed data is less. NGC 2403 shows a rapid drop of depletion at the outer radii, which cannot be explained by our models, however it is still consistent with our model up to $r/R_{25} \sim 0.5$.

Finally, we compare the galaxies in Category IV with the simulation at $t = 10$ Gyr in Fig. 16d. Our simulation broadly overestimates the observed data, and the slope is flatter than the observed data. The radial profile of depletion and $\mathcal{D}_{\rm tot}$ is flatter at $t = 10$ Gyr than at 3 Gyr. Because accretion is saturated at later times, the difference of $f_{\rm dense}$ does not affect the results significantly. Some galaxies in Category IV indeed have a flat profile of $\mathcal{D}_{\rm tot}/Z$, which is qualitatively consistent with our results.

6 CONCLUSION

In this paper, we investigate the time evolution and spatial distribution of dust in an isolated galaxy with a modified version of `GADGET-3` SPH code. To represent the grain size

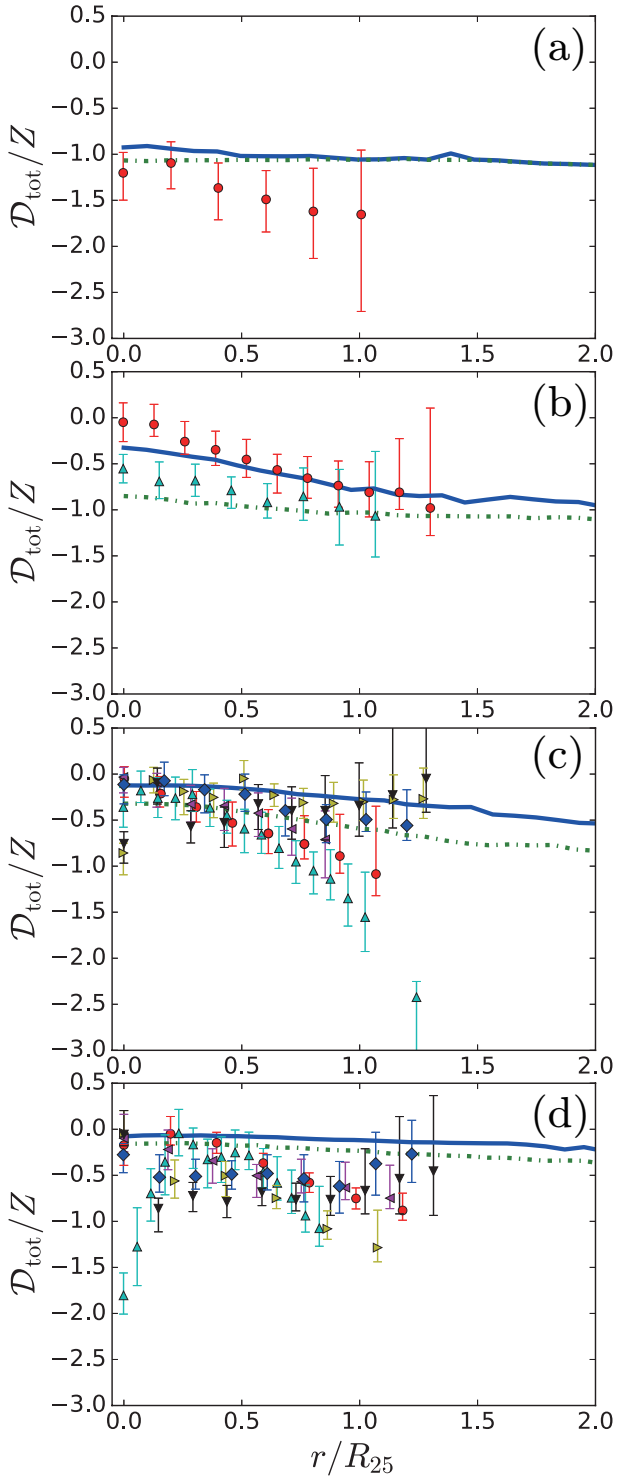

Figure 16. Comparison of simulation results with observed radial profiles of depletion in each category (panels (*a*) to (*d*) correspond to Category I to IV, respectively). The solid and dotted lines represent the cases with $f_{\rm dense} = 0.5$ and 0.1, respectively. The data points are obtained by Mattsson & Andersen (2012). The symbols for observational points indicate the same galaxies as Fig. 15.

distribution, we calculate the abundances of small and large grains separately based on the one-zone model by Hirashita (2015) Dust production by stars and destruction by SNe are implemented consistently with star formation. In order to overcome the mass resolution of the simulation, we develop subgrid models for accretion and coagulation, since these processes occur in dense clouds whose sizes are below the spatial resolution of the simulation.

We find that the assumption of fixed dust-to-metal mass ratio becomes no longer valid when the galaxy age is $\gtrsim 0.2$ Gyr, because the grain growth by accretion produces a nonlinear dependence of dust-to-gas ratio on the metallicity. Small grain production by shattering triggers accretion, because small grains are more efficient in accreting the gas-phase metals. In addition, coagulation becomes also significant at ages $\gtrsim 1$ Gyr after a large amount of small grains are produced by accretion. The age-dependent contributions of those processes are all important in driving the evolution of dust-to-gas ratio and grain size distribution at various epochs, and thus should be included in any calculation of dust evolution in galaxies.

Finally, we made a first attempt of comparing our simulation results with spatially resolved observational data of nearby galaxies. To extract the typical age in a simple way, we use the specific star formation rate (sSFR) as an indicator, and compared the observed radial profiles of dust-to-gas ratio and dust-to-metal ratio (i.e., depletion) with the simulation snapshots at various ages. We find that the radial profiles calculated in our models are broadly consistent with observations. The negative radial gradient of dust-to-gas ratio is explained by the tight relation between dust-to-gas ratio and metallicity. The radial profile of depletion is flat at early epochs ($t \lesssim 0.3$ Gyr), because the dust-to-metal ratio is simply determined by the dust condensation efficiency in stellar ejecta. At later stages, the radial gradient of depletion is negative, which represents the fact that the dust-to-gas ratio is a nonlinear (strong) function of metallicity due to accretion. We also reproduce the observational trend that the radial gradient of depletion becomes flatter as the galaxy is aged, which indicates that the regions with efficient grain growth by accretion extend from inside to outwards.

ACKNOWLEDGMENT

We are grateful to Volker Springel for providing us with the original version of GADGET-3 code, and to Akio Inoue and Hidenobu Yajima for useful discussions. This work was supported in part by JSPS KAKENHI Grant Number 26247022. HH thanks the Ministry of Science and Technology for support through grant MOST 105-2112-M-001-027-MY3. Numerical simulations were in part carried out on XC30 at the Centre for Computational Astrophysics, National Astronomical Observatory of Japan.

REFERENCES

Agertz O., Kravtsov A. V., Leitner S. N., Gnedin N. Y., 2013, ApJ, 770, 25

Asano R. S., Takeuchi T. T., Hirashita H., Inoue A. K., 2013a, Earth, Planets, and Space, 65, 213

Asano R. S., Takeuchi T. T., Hirashita H., Nozawa T., 2013b, MNRAS, 432, 637
Asano R. S., Takeuchi T. T., Hirashita H., Nozawa T., 2014, MNRAS, 440, 134
Barlow M. J., Silk J., 1976, ApJ, 207, 131
Bekki K., 2013, MNRAS, 432, 2298
Bekki K., 2015, MNRAS, 449, 1625
Bohren C. F., Huffman D. R., Kam Z., 1983, Nature, 306, 625
Bryan G. L., et al., 2014, ApJS, 211, 19
Buat V., Boselli A., Gavazzi G., Bonfanti C., 2002, A&A, 383, 801
Calzetti D., Armus L., Bohlin R. C., Kinney A. L., Koornneef J., Storchi-Bergmann T., 2000, ApJ, 533, 682
Cazaux S., Spaans M., 2009, A&A, 496, 365
Cazaux S., Tielens A. G. G. M., 2004, ApJ, 604, 222
Chabrier G., 2003, PASP, 115, 763
Chevalier R. A., 1974, ApJ, 188, 501
Choi J.-H., Nagamine K., 2009, MNRAS, 393, 1595
Choi J.-H., Nagamine K., 2012, MNRAS, 419, 1280
Draine B. T., Li A., 2001, ApJ, 551, 807
Durier F., Dalla Vecchia C., 2012, MNRAS, 419, 465
Dutta P., Begum A., Bharadwaj S., Chengalur J. N., 2013, New Astron., 19, 89
Dwek E., 1998, ApJ, 501, 643
Elmegreen D. M., 1998, Galaxies and galactic structure. Upper Saddle River, NJ : Prentice Hall
Fall S. M., Krumholz M. R., Matzner C. D., 2010, ApJ, 710, L142
Gould R. J., Salpeter E. E., 1963, ApJ, 138, 393
Heesen V., Brinks E., Leroy A. K., Heald G., Braun R., Bigiel F., Beck R., 2014, AJ, 147, 103
Hirashita H., 2015, MNRAS, 447, 2937
Hirashita H., Kuo T.-M., 2011, MNRAS, 416, 1340
Hirashita H., Voshchinnikov N. V., 2014, MNRAS, 437, 1636
Hirashita H., Yan H., 2009, MNRAS, 394, 1061
Hopkins P. F., 2013, MNRAS, 428, 2840
Hopkins P. F., Quataert E., Murray N., 2011, MNRAS, 417, 950
Hou K.-C., Hirashita H., Michałowski M. J., 2016, preprint, (arXiv:1608.06099)
Inoue A. K., 2011a, Earth, Planets, and Space, 63, 1027
Inoue A. K., 2011b, MNRAS, 415, 2920
Jaacks J., Nagamine K., Choi J. H., 2012, MNRAS, 427, 403
Jaacks J., Thompson R., Nagamine K., 2013, ApJ, 766, 94
Jones A. P., Tielens A. G. G. M., Hollenbach D. J., McKee C. F., 1994, ApJ, 433, 797
Jones A. P., Tielens A. G. G. M., Hollenbach D. J., 1996, ApJ, 469, 740
Kataoka A., Okuzumi S., Tanaka H., Nomura H., 2014, A&A, 568, A42
Kennicutt R. C., Evans N. J., 2012, ARA&A, 50, 531
Kim J.-h., et al., 2014, ApJS, 210, 14
Kuo T.-M., Hirashita H., 2012, MNRAS, 424, L34
Kuo T.-M., Hirashita H., Zafar T., 2013, MNRAS, 436, 1238
Larson R. B., 2005, MNRAS, 359, 211
Li A., Draine B. T., 2001, ApJ, 554, 778
Mathis J. S., 1990, ARA&A, 28, 37
Mathis J. S., Rumpl W., Nordsieck K. H., 1977, ApJ, 217, 425
Mattsson L., Andersen A. C., 2012, MNRAS, 423, 38
McKee C., 1989, in Allamandola L. J., Tielens A. G. G. M., eds, IAU Symposium Vol. 135, Interstellar Dust. p. 431
McKee C. F., Ostriker J. P., 1977, ApJ, 218, 148
McKee C. F., Hollenbach D. J., Seab G. C., Tielens A. G. G. M., 1987, ApJ, 318, 674
McKinnon R., Torrey P., Vogelsberger M., Hayward C. C., Marinacci F., 2016a, preprint, (arXiv:1606.02714)
McKinnon R., Torrey P., Vogelsberger M., 2016b, MNRAS, 457, 3775
Morris J. P., 1996, Publ. Astron. Soc. Australia, 13, 97
Moustakas J., Kennicutt Jr. R. C., Tremonti C. A., Dale D. A., Smith J.-D. T., Calzetti D., 2010, ApJS, 190, 233
Nagamine K., Fukugita M., Cen R., Ostriker J. P., 2001, ApJ, 558, 497
Nagamine K., Springel V., Hernquist L., Machacek M., 2004, MNRAS, 350, 385
Nozawa T., Fukugita M., 2013, ApJ, 770, 27
Nozawa T., Kozasa T., Habe A., 2006, ApJ, 648, 435
Nozawa T., Asano R. S., Hirashita H., Takeuchi T. T., 2015, MNRAS, 447, L16
Okuzumi S., Tanaka H., Sakagami M.-a., 2009, ApJ, 707, 1247
Omukai K., Tsuribe T., Schneider R., Ferrara A., 2005, ApJ, 626, 627
Rémy-Ruyer A., et al., 2014, A&A, 563, A31
Saitoh T. R., Makino J., 2013, ApJ, 768, 44
Sandstrom K. M., et al., 2013, ApJ, 777, 5
Schaye J., et al., 2015, MNRAS, 446, 521
Schneider R., Omukai K., Inoue A. K., Ferrara A., 2006, MNRAS, 369, 1437
Shimizu I., Inoue A. K., Okamoto T., Yoshida N., 2014, MNRAS, 440, 731
Shimizu I., Inoue A. K., Yoshida N., Okamoto T., 2015, preprint, (arXiv:1509.00800)
Smith M. W. L., et al., 2016, MNRAS, 462, 331
Springel V., 2005, MNRAS, 364, 1105
Springel V., Hernquist L., 2002, MNRAS, 333, 649
Springel V., Hernquist L., 2003, MNRAS, 339, 289
Steidel C. C., Adelberger K. L., Giavalisco M., Dickinson M., Pettini M., 1999, ApJ, 519, 1
Stinson G. S., Brook C., Macciò A. V., Wadsley J., Quinn T. R., Couchman H. M. P., 2013, MNRAS, 428, 129
Takeuchi T. T., Buat V., Heinis S., Giovannoli E., Yuan F.-T., Iglesias-Páramo J., Murata K. L., Burgarella D., 2010, A&A, 514, A4
Takeuchi T. T., Yuan F.-T., Ikeyama A., Murata K. L., Inoue A. K., 2012, ApJ, 755, 144
Thompson R., Nagamine K., Jaacks J., Choi J.-H., 2014, ApJ, 780, 145
Todoroki K., 2014, Master's thesis, University of Nevada, Las Vegas
Valiante R., Schneider R., Bianchi S., Andersen A. C., 2009, MNRAS, 397, 1661
Vogelsberger M., et al., 2014, MNRAS, 444, 1518
Voshchinnikov N. V., Hirashita H., 2014, MNRAS, 445, 301
Whitworth A. P., Boffin H. M. J., Francis N., 1998, MNRAS, 299, 554
Wise J. H., Abel T., Turk M. J., Norman M. L., Smith B. D., 2012, MNRAS, 427, 311
Woosley S. E., Heger A., 2007, Phys. Rep., 442, 269
Yajima H., Nagamine K., Thompson R., Choi J.-H., 2014, MNRAS, 439, 3073
Yajima H., Shlosman I., Romano-Díaz E., Nagamine K., 2015, MNRAS, 451, 418
Yamasawa D., Habe A., Kozasa T., Nozawa T., Hirashita H., Umeda H., Nomoto K., 2011, ApJ, 735, 44
Yan H., Lazarian A., Draine B. T., 2004, ApJ, 616, 895
Zhou Z.-M., Cao C., Wu H., 2015, AJ, 149, 1
Zhukovska S., 2014, A&A, 562, A76
Zhukovska S., Gail H.-P., Trieloff M., 2008, A&A, 479, 453
Zhukovska S., Dobbs C., Jenkins E. B., Klessen R., 2016, preprint, (arXiv:1608.04781)
de Blok W. J. G., Walter F., Brinks E., Trachternach C., Oh S.-H., Kennicutt Jr. R. C., 2008, AJ, 136, 2648
de Vaucouleurs G., Pence W. D., 1978, AJ, 83, 1163

APPENDIX A: DESTRUCTION OF NEWLY PRODUCED DUST

We consider SNe occurring in a newly formed stellar particle in the simulation. The number of SNe is denoted as N, which is estimated in eq. (18) . For simplicity, we assume that each SN provides mass $\Delta M_{\rm d}^{(1)}$ of dust, which is evaluated as

$$\Delta M_{\rm d}^{(1)} = \frac{1}{N} \times f_{\rm in} \mathcal{Y}'_{\rm Z} \Delta M_{\rm return} \, . \tag{A1}$$

Since there is no spatially resolved information within each gas particle, we assume that the dust produced by SNe is instantaneously distributed to the surrounding gas particles according to the kernel function. The dust which was produced by the first SN in the gas particle would suffer from the shocks of subsequent $N-1$ SNe. In general, the dust produced by the i-th SN in the particle experiences destruction by $N-i$ shocks.

As estimated in Section 2.2, each SN destroys a fraction $\varepsilon m_{\rm sw}/m_{\rm g}$ of dust within the gas particle. Thus, if we define the surviving fraction as $\eta_{\rm s} \equiv 1 - \varepsilon_{\rm SN} m_{\rm sw}/m_{\rm g}$ ($0 < \eta_{\rm s} < 1$ in our simulation), the net increase of dust after destruction is

$$\Delta M'_{\rm d} = \Delta M_{\rm d}^{(1)} \sum_{k=0}^{N-1} \eta_{\rm s}^k = \begin{cases} \Delta M_{\rm d}^{(1)} \dfrac{1-\eta_{\rm s}^N}{1-\eta_{\rm s}} \ (\text{for } N \geq 2) \\ \Delta M_{\rm d}^{(1)} \ (\text{for } N = 1) \, . \end{cases} \tag{A2}$$

By using eq. (A1), we obtain $\Delta M'_{\rm d}$ as

$$\Delta M'_{\rm d} = \begin{cases} \dfrac{1}{N} \times f_{\rm in} \mathcal{Y}'_{\rm Z} \Delta M_{\rm return} \dfrac{1-\eta_{\rm s}^N}{1-\eta_{\rm s}} \ (\text{for } N \geq 2) \\ f_{\rm in} \mathcal{Y}'_{\rm Z} \Delta M_{\rm return} \ (\text{for } N = 1). \end{cases} \tag{A3}$$

On the other hand, $\Delta M'_{\rm d}$ can also be written with the destroyed fraction δ as

$$\Delta M'_{\rm d} = f_{\rm in} \mathcal{Y}'_{\rm Z} \Delta M_{\rm return} (1-\delta) \, . \tag{A4}$$

By combining eq. (A3) with eq. (A4), we obtain

$$(1-\delta) = \begin{cases} \dfrac{1}{N} \dfrac{1-\eta_{\rm s}^N}{1-\eta_{\rm s}} \ (\text{for } N \geq 2) \, , \\ 1 \ (\text{for } N = 1) \, . \end{cases} \tag{A5}$$

APPENDIX B: DERIVATION OF THE TIME-SCALE OF COLLISIONAL PROCESS

For grain-grain collisional processes such as coagulation and shattering, the time-scales are estimated based on the collision time-scale $\tau_{\rm coll}$. This time-scale can be estimated by

$$\tau_{\rm coll} = \frac{1}{\sigma v n_{\rm d}} \, , \tag{B1}$$

where v, σ and $n_{\rm d}$ are the typical velocity dispersion, the cross section and the number density of the dust grains, respectively. The cross section can be estimated as

$$\sigma \simeq \pi a^2 \, , \tag{B2}$$

where a is the grain radius (we assume spherical grains). For convenience, we express $n_{\rm d}$ with the dust-to-gas ratio, $\mathcal{D}$,

$$n_{\rm d} = \frac{\mathcal{D} \mu m_{\rm H} n_{\rm H}}{\frac{4}{3} \pi a^3 s} , \tag{B3}$$

where $\mu = 1.4$ is the mean weight of gas particles per hydrogen, $m_{\rm H}$ is the hydrogen mass (i.e. $\mu m_{\rm H}$ is the gas mass per hydrogen nucleus), and s is the material density of the dust. Using the dust-to-gas ratio, the collision time-scale is expressed as

$$\begin{aligned} \tau_{\rm coll} &= \frac{\frac{4}{3} a s}{v \mathcal{D} \mu m_{\rm H} n_{\rm H}} \\ &= 5.41 \times 10^7 \left(\frac{\mathcal{D}}{0.01} \right)^{-1} \left(\frac{n_{\rm H}}{1 \ {\rm cm}^{-3}} \right)^{-1} \left(\frac{a}{0.1 \ \mu{\rm m}} \right) \\ &\quad \times \left(\frac{s}{3 \ {\rm g \ cm}^{-3}} \right) \left(\frac{v}{10 \ {\rm km \ s}^{-1}} \right)^{-1} [{\rm yr}] \, . \end{aligned} \tag{B4}$$

This paper has been typeset from a TEX/LATEX file prepared by the author.